# FINITE ELEMENT ANALYSIS INVESTIGATING THE SLIDING CONTACT OF A SHAPE MEMORY ALLOY SUBSTRATE

A Thesis

by

RALSTON IGNATIUS TARSICO FERNANDES

Submitted to the Office of Graduate and Professional Studies of
Texas A&M University
in partial fulfillment of the requirements for the degree of

MASTER OF SCIENCE

| | |
|---|---|
| Chair of Committee, | James G. Boyd |
| Co-Chair of Committee, | Dimitris C. Lagoudas |
| Committee Members, | Sami El-Borgi |
| Head of Department, | Rodney Bowersox |

August 2018

Major Subject: Aerospace Engineering

# ABSTRACT

Recent experimental wear tests have demonstrated that shape memory alloys offer better wear resistance than conventional wear resistant materials and therefore make them ideal candidates as tribological materials. The wear resistance of shape memory alloys has been attributed to its pseudoelasticity and high yield strength. To date however, an extensive computational study that simulates the contact behavior of these alloys during a typical sliding wear process has not been investigated.

This study uses the finite element method to analyze the sliding contact behavior between a rigid cylinder and a two dimensional shape memory alloy semi-infinite half-space. An experimentally validated constitutive model is used to capture the pseudoelastic effect exhibited by these alloys. The finite element contact model is validated with closed form solutions for well known normal and sliding elastic contact problems. Parametric studies involving key shape memory alloy material parameters (maximum recoverable transformation strain, the inherent difference between the elastic moduli of martensite and austenite phase, various isothermal loading paths) and coefficients of friction are conducted to study the effects on the sliding response. It is shown that the sliding response of SMAs is strongly temperature dependent, with significant residual stresses present in the half-space at temperatures below the austenitic finish temperature. An increase in the maximum transformation strain causes the stress distribution to be spread over a wider area and causes a significant decrease in the maximum von Mises stress in the half-space. The ability of shape memory alloys to undergo a stress induced transformation to a more compliant phase, also causes a reduction in the Mises stress and further demonstrates why pseudoelastic SMAs offer better wear resistance that conventional wear resistant materials.

*To my parents for their selfless love and sacrifice*

*and my sister for her love, support and companionship*

# ACKNOWLEDGMENTS

This thesis represents a significant milestone in my journey towards life-long learning and it would be remiss of me not to acknowledge the people who have aided me in this endeavor. First, I'd like to thank all my committee members for giving me the opportunity to widen my knowledge and make a contribution to the engineering sciences. I am constantly humbled by their extensive knowledge of engineering and their ability to effortlessly explain seemingly nebulous concepts. Dr. Boyd's guidance and mentorship was instrumental in the successful completion of this thesis. His understanding, patience and suggestions were invaluable in moments when it seemed like any attempt to produce satisfactory results appeared fruitless. I would like to thank Dr. Lagoudas for his insightful suggestions and for bringing me into the fold of his research group at Texas A&M. His weekly group meetings made me realize that while delivering results is important, it is equally important to be able to thoroughly understand and effectively communicate them. My sincere gratitude goes to Dr. El-Borgi at Texas A&M University at Qatar for taking me on as a research assistant fresh after graduating with my Bachelor's degree. His trust and encouragement spurred me on to become a better researcher and the knowledge and skills I gained under his guidance helped me seamlessly transition into graduate school.

In addition to my research mentors, my friends and colleagues in the Shape Memory Alloy Research Team deserve thanks as well. A special thanks goes out to Dr. Alexandros Solomou who provided both the hardware and software that was required to complete my research and always made time to provide helpful suggestions whenever I encountered difficulties with the technical minutiae of the finite element code. I would also like to thank my officemates from the S.M.A.R.T group Behrouz Haghgouyan, Jobin Joy, Dimitris Loufakis, Mahdi Mohajeri and Tianyang Zhou for being my sounding board when it came to brainstorming ideas to fix some of the numerous problems I faced and for interjecting several moments of much needed levity in my day to day struggles as a graduate student. My journey as a student has been enriched with their presence and I'm grateful for their help and support over these past few years.

I would also like to acknowledge the financial support for my graduate studies provided by the Aerospace Department at Texas A&M. Serving as a teaching assistant over the past two years introduced me to one of the most important aspects of academia and instilled in me a deeper respect for my professors and the rigors that accompany their teaching duties.

Finally, on a more personal note, my deepest gratitude is reserved for the most indispensable people in my life, my family, without whom I would never have made it thus far. I am eternally grateful for their selfless emotional support when it seemed like I could not achieve what I had set out to do and their moral support whenever I lost faith in my abilities. Whatever I have accomplished in life is a result of their hard work and sacrifice and for that I can never thank them enough.

CONTRIBUTORS AND FUNDING SOURCES

## Contributors

This work was supported by a thesis committee consisting of Professor James G. Boyd and Professor Dimitris C. Lagoudas of the Department of Aerospace Engineering and Professor Sami El-Borgi of the Department of Mechanical Engineering.

The shape memory alloy user material subroutine used to generate the results in Section 3 was developed by Dr. Alexandros Solomou, a post-doctoral research associate in the Department of Aerospace Engineering.

All other work conducted for the thesis was completed by the student independently.

## Funding Sources

Graduate study was supported by a teaching assistantship from the Department of Aerospace Engineering at Texas A&M University.

TABLE OF CONTENTS

Page

ABSTRACT ..... ii

DEDICATION ..... iii

ACKNOWLEDGMENTS ..... iv

CONTRIBUTORS AND FUNDING SOURCES ..... vi

TABLE OF CONTENTS ..... vii

LIST OF FIGURES ..... ix

LIST OF TABLES ..... xii

1. INTRODUCTION ..... 1

    1.1 Literature Review ..... 2
        1.1.1 Elastic Contact ..... 2
        1.1.2 Inelastic Contact ..... 4
        1.1.3 Shape Memory Alloys ..... 6
        1.1.4 Contact Mechanics of Shape Memory Alloys ..... 8
        1.1.5 Wear Behavior of Shape Memory Alloys ..... 11
    1.2 Research Objectives and Thesis Outline ..... 13

2. MODELING FRAMEWORK ..... 15

    2.1 Key Assumptions ..... 15
    2.2 Shape Memory Alloy Constitutive Model ..... 16
    2.3 Contact Model ..... 20
    2.4 Finite Element Model ..... 21
    2.5 Mesh Domain Convergence ..... 23
    2.6 Model Validation ..... 25
        2.6.1 Normal Contact ..... 26
        2.6.2 Sliding Contact ..... 29
        2.6.3 Onset of Phase Transformation ..... 31

3. PARAMETRIC STUDY ..... 34

    3.1 Effect of Temperature ..... 35
    3.2 Effect of Maximum Recoverable Transformation Strain ..... 45

3.3 Effect of Modulus Change ..... 53
3.4 Effect of Friction ..... 57

4. CONCLUSIONS AND FURTHER STUDIES ..... 63

4.1 Conclusion ..... 63
4.2 Further Study ..... 65

REFERENCES ..... 66

LIST OF FIGURES

FIGURE Page


1.1 Hertzian contact of two spheres. ..... 2

1.2 Typical sliding contact showing normal traction $P$ and tangential traction $Q$. ..... 4

1.3 SMA phase diagram and pseudoelastic stress-strain response. ..... 7

1.4 Typical shape memory effect loading path [1]. ..... 8

2.1 Two dimensional pseudoelastic half-space in contact with a rigid cylinder of radius $R$ (lower half shown). ..... 22

2.2 Half-Space Domain convergence study where the height $H$ of the domain is varied from $2R - 14R$, the length $L = 2H$. ..... 24

2.3 Contact region element size convergence study. ..... 25

2.4 Normal contact of a rigid cylinder on an elastic half-space. ..... 27

2.5 Comparison of contact pressure distribution (Analytical vs. FEM). ..... 28

2.6 Comparison of sub-surface stress distribution in the half-space along $x/a = 0$ ($F = 1.25$ N/mm, $\mu = 0$). ..... 29

2.7 Comparison of sub-surface stress distribution in the half-space along left($x = 0$) and right ($x = 0.9354a$),($F = 1.25$N/mm, $\mu = 0.15$). ..... 31

2.8 Comparison between FEM and analytical predictions for the critical normal distributed force to initiate transformation in the half-space for a range of temperatures. 33

3.1 SMA constitutive response at different temperatures. ..... 36

3.2 Reaction forces on the indenter at different isothermal loading paths throughout the frictionless sliding process (a) tangential distributed force (b) normal distributed force. ..... 37

3.3 Normalized $\sigma_{VM}$ (top) and $\xi$ (bottom) in the half-space during different stages of sliding contact for $T > A_f$. ..... 39

3.4 Normalized $\sigma_{VM}$ (top) and $\xi$ (bottom) in the half-space during different stages of sliding contact for $A_f < T < A_s$. ..... 40

3.5 Normalized $\sigma_{VM}$ (top) and $\xi$ (bottom) in the half-space during different stages of sliding contact for $A_s < T$. ..... 41

3.6 Comparison of surface displacements at different isothermal loading paths after (a) indentation and during (b) steady state sliding. ..... 42

3.7 Comparison of the contact pressure distribution at different isothermal loading paths after (a) indentation and during (b) steady state sliding. ..... 43

3.8 Constitutive response when $H^{max}$ is varied from 1% -4%. ..... 45

3.9 Reaction forces on the indenter at different half-space maximum transformation strains $H^{max}$ throughout the frictionless sliding process (a) tangential distributed force (b) normal distributed force. ..... 46

3.10 Normalized von Mises stress in the pseudoelastic half-space after indentation for various $H^{max}$ values (1%-4%) at an indentation depth of $\Delta y = 0.008R \approx 0.15a$. ... 48

3.11 Martensite volume fraction in the pseudoelastic half-space after indentation for various $H^{max}$ values (1%-4%) at an indentation depth of $\Delta y = 0.008R \approx 0.15a$. ... 49

3.12 Normalized von Mises stress in the pseudoelastic half-space at steady state sliding for various $H^{max}$ values (1%-4%) at an indentation depth of $\Delta y = 0.008R \approx 0.15a$. 50

3.13 Martensite volume fraction in the pseudoelastic half-space at steady-state sliding for various $H^{max}$ values (1%-4%) at an indentation depth of $\Delta y = 0.008R \approx 0.15a$. 51

3.14 Comparison of the contact pressure distribution for various $H^{max}$ values (1%-4%) after (a) indentation and during (b) steady state sliding. ..... 52

3.15 Constitutive response for different $\beta = \frac{E_M}{E_A}$. ..... 54

3.16 Normalized von Mises stress and martensite volume fraction in the pseudoelastic half-space after indentation for various $\beta$ values.($\Delta y = 0.008R \approx 0.15a$, $H^{max} = 2\%$, $T = 285K$). ..... 55

3.17 Normalized von Mises stress and martensite volume fraction in the pseudoelastic half-space during steady state sliding for various $\beta$ values. ($\Delta y = 0.008R \approx 0.15a$, $H^{max} = 2\%$, $T = 285K$). ..... 56

3.18 Comparison of the contact pressure distribution for various elastic mismatch ratios after (a) indentation and during (b) steady state sliding. ..... 57

3.19 Comparison of the von Mises stress distribution in an elastic half-space for various friction coefficients $\mu$ at steady state sliding ($\Delta x/R = 0.00275$). ..... 58

3.20 Normalized von Mises stress (left) and martensite volume fraction (right) in the pseudoelastic half-space for various friction coefficients $\mu$ at steady state sliding ($\Delta x/R = 0.00275, T = 285\text{K} > A_f$). ..... 60

3.21 Normalized von Mises stress (left) and martensite volume fraction (right) in the pseudoelastic half-space for various friction coefficients $\mu$ at steady state sliding ($\Delta x/R = 0.00275, T = 275\text{ K} < A_f$). ..... 61

3.22 Normalized von Mises stress (left) and martensite volume fraction (right) in the pseudoelastic half-space for various friction coefficients $\mu$ at steady state sliding ($\Delta x/R = 0.00275, T = 265\text{ K} < A_s$). ..... 62

LIST OF TABLES

TABLE Page

3.1 Relevant Model Parameters. . . . . 35

3.2 Normalized maximum von Mises stress $\sigma_{VM}/\sigma_{VM,El}^{max}$ at indentation and at steady state sliding for different isothermal loading paths ($H^{max} = 2\%, \mu = 0$). . . . . 42

3.3 Normalized maximum von Mises stress $\sigma_{VM}/\sigma_{VM,El}^{max}$ at indentation and at steady state sliding for different $H^{max}$ values ($T$=285 K,$\mu = 0$). . . . . 51

3.4 Normalized maximum von Mises stress $\sigma_{VM}/\sigma_{VM,El}^{max}$ at indentation and at steady state sliding for different $\beta$ values ($T$=285 K,$\mu = 0$,$H^{max} = 2\%$). . . . . 56

3.5 Normalized maximum von Mises stress $\sigma_{VM}/\sigma_{VM,El}^{max}$ at steady state sliding for different $\mu$ values ($H^{max} = 1\%$, $\beta = 0.84$). . . . . 62

# 1. INTRODUCTION

Contact mechanics is a branch of applied mechanics that focuses on the stresses and deformation of two or more bodies undergoing surface interactions, as a result of internal and/or external loads. Contact mechanics has several applications in various industries across multiple scales and has led to the development of a new branch of engineering called tribology that focuses on the wear and lubrication of bodies in contact. Some examples include the locomotive industry, where the macroscopic contacts of wheel on rails, gears, bearings, brakes and tires need to be studied so as to extend their life under repeated severe contact; the oil and gas industry, where the fretting wear due to reciprocating contact at the gas turbine blade and disk interface is a critical issue that decreases the energy transfer efficiency and gas turbine lifetime; the biomedical industry, where the design and material selection of artificial implants and joints that undergo severe and repeated contact with other body parts is critical and the nano/micro-electronic-mechanical system (N/MEMS) industry, where surface roughness and the geometry of asperities at these small scales need to considered to ensure repeatable and reliable contact and to avoid mechanical failure like stiction and wear. It has also served as the foundation for academic research in the field of nanoindentation, wherein material properties such as hardness and elastic moduli of nanoscale thin films can be determined using principles of elastic contact mechanics.

The importance of material selection in the prevention of various contact driven failure modes such as wear and crack propagation cannot be understated. Several experimental studies have recently demonstrated excelled wear resistant properties of a new class of material called shape memory alloys (SMA). This material possesses a thermo-mechanical coupling and undergoes a phase transformation during a typical sliding wear process. To date however, the literature on simulating the contact behavior of this unique material in a typical sliding wear process is limited and needs to be explored so as to further leverage its unique wear resistant properties.

The following sections will review the basics of elastic contact mechanics and will address the challenges involved in studying the contact mechanics of materials that demonstrate an inelastic

constitutive behavior. An overview of the thermo-mechanical inelastic behavior (pseudoelasticity, shape memory) of shape memory alloys is provided and relevant literature conducted to study the contact mechanics of these specific materials is discussed. A literature review on the implications of pseudoelasticity on the experimental wear behavior of shape memory alloys is also provided. Finally a general outline of this thesis and its research objectives will be presented.

## 1.1 Literature Review

### 1.1.1 Elastic Contact

The seminal study in the field of contact mechanics was conducted by Hertz [2] towards the close of the 19th century. Hertz introduced analytical solutions for three dimensional normal contact of non-conforming spheres, with each possessing dissimilar radii and isotropic elastic material properties (Figure 1.1). The solution for the stress field in the two bodies resulting from this contact was later provided by Huber [3]. In the development of these analytical solutions, it was assumed that the contacting surfaces are in perfect slip (i.e. frictionless). The Hertzian model is powerful in the sense that certain simplifications can be introduced to study a range of contact problems such as a rigid sphere in normal contact with an elastic semi-infinite half-space or an elastic sphere in normal contact with an elastic semi-infinite half-space. The Hertzian contact model can also be generalized to a two-dimensional plane strain and plane stress analysis [4].

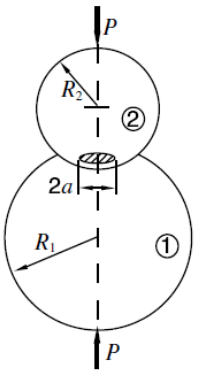


Figure 1.1: Hertzian contact of two spheres.

While the Hertzian model is only applicable to contact between spherical bodies, analytical solutions for the stress field due to plane contact between a rigid body of a specific profile and an elastic half-space are also available. The origin of these solutions are rooted in the point contact solutions in 3-D formulated by Boussinesq [5] and the line contact solutions in 2-D developed by Flamant [6]. By using the principle of superposition, the Boussinesq solution for a point contact allows the stress distribution in the elastic half-space to be determined for any distribution of pressure within a contact area. This approach has resulted in closed-form solutions for contact between an elastic half-space and a rigid cylinder, rigid cone/wedge and rigid flat punch since the contact pressure distribution for these geometries is known a-priori [4], [7].

Contacting bodies that slide relative to each other are considered to be in sliding contact. In well lubricated bodies, frictional forces and tangential tractions are absent and therefore the stress field in the half-space is unaffected by the sliding motion. In the case of dry frictional sliding, tangential forces arise that oppose the direction of the prescribed sliding motion. Sliding contact mechanics is therefore concerned with the stresses and deformation of the half-space due to the combined presence of normal and tangential tractions (Figure 1.2). A limiting value of the tangential traction required to initiate perfect slip during sliding is described using Amonton's law, which relates the normal traction to the tangential traction via the coefficient of friction. The coefficient of friction is defined as the ratio of the tangential traction to the normal traction and its value typically does not exceed unity [4]. If the specified tangential traction is above this limiting value in the contact region, then the sliding contact is said to be in perfect slip, else if the entire contact region is below this limiting value, the sliding contact is in perfect stick. As a result of the tangential traction during frictional sliding, the symmetry of the subsurface stress distribution during a typical Hertzian type of contact disappears. In addition the level of stress at any given depth increases and gradually moves closer toward the loaded surface. Analytical solutions for the stress field generated due to an elastic cylinder in sliding contact with an elastic half-space are provided by several authors [8–10] and for an elastic sphere on an elastic half-space by other authors [11, 12]. For the case of a rigid cone in sliding contact with an elastic half-space, a framework to determine the explicit solutions

for the stress distribution in the elastic half-space is provided by [13], however the authors note that in practice, because of the stress singularity at the cone tip, plasticity commences immediately once the cone indents and slides along the half-space.

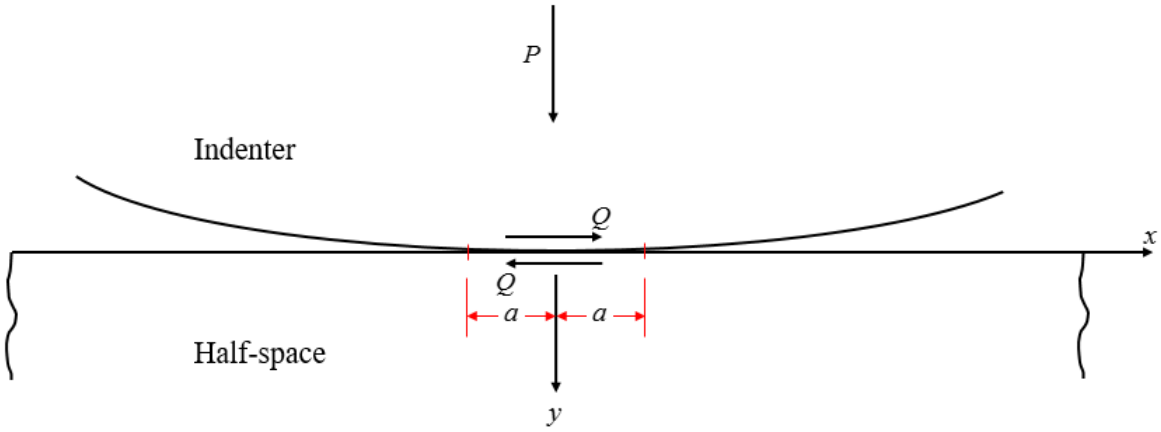


Figure 1.2: Typical sliding contact showing normal traction $P$ and tangential traction $Q$.

### 1.1.2 Inelastic Contact

The previous section outlined classical contact mechanics solutions for axi-symmetric indenters on semi-infinite half-spaces as well as 2-D simplifications for some contact problems. In reality, contact between two bodies rarely occurs between axi-symmetric indenters and infinite bodies. Furthermore, contact between bodies often extends beyond the elastic regime, either because the applied loads are high enough to initiate plastic yield or due to stress singularities associated with the geometry of the indenter. By applying the von Mises or Tresca failure criterion to the Hertzian contact solutions for a sphere or a cylinder on a half-space, it is possible to predict the onset of failure [4]. For instance, Green [14] used the von Mises criteria to predict the critical load, contact area and maximum indentation depth at the onset of plasticity when two cylinders and spheres come in contact.

Some approximate solutions for the mean contact pressure between a rigid indenter and a rigid-

perfectly plastic material have been solved by means of the slip-line field theory [4, 15]. These solutions are typically used to determine an approximate value for the hardness of metals and are only applicable for the case when the plastic region completely surrounds the contact region and elastic effects in the rest of the half-space do not have a significant effect.

To date, a complete analytical solution for the stress distribution of an elastic-plastic half-space with a rigid indenter of the various geometries considered in the elastic contact case have not been solved. This is because the shape and the size of the elastic-plastic boundary are not known a-priori [4]. Researchers have therefore resorted to studying the elastic-plastic contact problem using semi-analytical or numerical techniques such as the finite element method (FEM). Because of the breadth of work since the advent of FEM, only the literature on elastic-plastic contact problems of relevance to the current work (two-dimensional normal and sliding contact) are discussed. A detailed review on this topic has been very recently summarized by Ghaednia et al. [16] that covers the 2D plane strain/plane stress and 3D axisymmetric normal and sliding contact of elastic-plastic materials.

In one of the first studies, Dumas and Baronet [17] studied the plane-strain normal contact (indentation) between a cylinder and an elastic-plastic half-space with the different hardening slopes using the finite element method. The residual depths upon unloading were compared with experimental observations to agreeable results. They also showed that as the plasticity in the half-space increases, the contact pressure distribution changes from an elliptical shape to a flattened shape. A similar flattening behavior of the contact pressure distribution using FEM was also obtained by Carre and Fisher-Cripps [18] and Komvopoulos [19], who studied the indentation problem of a layered half-space. This flattening behavior of the contact pressure distribution was attributed to large plastic strains either in the region of contact or directly beneath the region of contact. Since then, several authors have studied the 2-D sliding contact of a cylinder on a layered half-space and showed that the presence of a hard layer on a soft substrate can prevent surface yielding even at high coefficients of friction [20–22].

### 1.1.3 Shape Memory Alloys

Over the last three decades, there has been a growing academic and commercial interest in multi-functional materials. These materials possess a coupling between different forms of energy. Examples of these materials include piezoelectric materials that couple electrical and mechanical energy; thermoelectric materials that couple thermal and electrical effects and shape memory materials that can couple thermal and mechanical energy. Among these various classes of multi-functional materials, Shape Memory Alloys (SMAs) possess the highest actuation work density [1].

This coupling between thermal and mechanical energy demonstrated by SMAs physically manifests itself in the form of large macroscopic deformations resulting from a change in the constituent material phase of the SMA. This phase change or phase transformation occurs as a result of atomic lattice shearing when the SMA transitions between its high temperature austenite phase to a low temperature martensite phase and is triggered either by a change in stress, temperature or a combination thereof. Each phase has its own crystal structure and mechanical properties. For instance, the martensite phase can exist is different crystal lattice configurations such as orthorhombic, tetragonal or monoclinic while the austenitic phase is generally cubic. The reversible transformation between phases has produced uses for SMA materials in a number of fields including aerospace [23–26], biomedical [27, 28], and many others [29, 30].

Figure 1.3 and Figure 1.4 demonstrate the two most relevant thermomechanical paths in stress-temperature space which produce macroscopic deformation in SMA materials and are of importance for a typical contact mechanics problem. If an SMA that is initially in the high temperature austenite phase is cooled at zero stress, then phase change to martensite initiates at the temperature $M_s$ and completes at $M_f$. The martensite crystals formed at this zero load cooling step are self-accommodating in nature (twinned). Heating the SMA causes reverse transformation to austenite to initiate at $A_s$ and finish at $A_f$. If these cooling and heating steps are performed at non-zero isobaric conditions, the transformation temperatures $M_s, M_f, A_s$, and $A_f$ shift and accordingly a phase diagram can be built as shown in Figure 1.3. This shift in the transformation temperatures

varies almost linearly with the applied load and the slope of this thermo-mechanical coupling for each phase is represented in the phase diagram as $C_M$ and $C_A$. The black dashed lines in the diagrams are associated with the material twinning where below $\sigma_s$, martensite is in the twinned state and above $\sigma_f$, the vast majority of martensite variants are detwinned. The two most common thermomechanical paths taken by SMAs under typical contact applications are described as follows:

- Pseudoelastic Path

  The SMA initially in the austenite phase is increasingly stressed in an isothermal environment until phase change into martensite occurs. The material is then unloaded back to austenite. The transformation from austenite to martensite occurs at a specific stress $\sigma_{Ms}$ and completes at a higher stress $\sigma_{Mf}$.

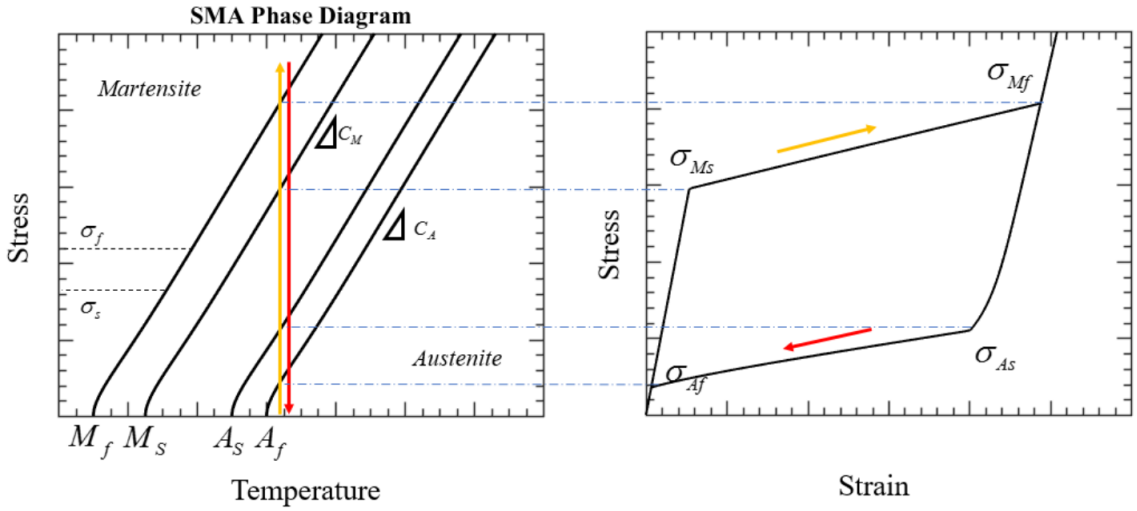


Figure 1.3: SMA phase diagram and pseudoelastic stress-strain response.

The SMA unloads elastically until it hits a critical stress $\sigma_{As}$ at which point it begins to transforms back to austenite. A complete transformation to austenite is achieved when the stress reaches $\sigma_{Af}$. This path is typically used for damping applications where the phase change

is able to absorb energy put into the systems. It also forms the basis for the mechanical behavior of the SMA in the contact mechanics problem presented in this thesis.

- Shape Memory Path

  Material initially in the austenitic phase is cooled to martensite at zero stress, then loaded above $\sigma_f$ to induce detwinning in the martensitic phase and achieve a macroscopic deformation. The material is then unloaded and an apparent permanent deformation is observed. Upon heating to a temperature above $A_f$, the material reverts back into the austenite phase and a recovery of the original configuration is observed.

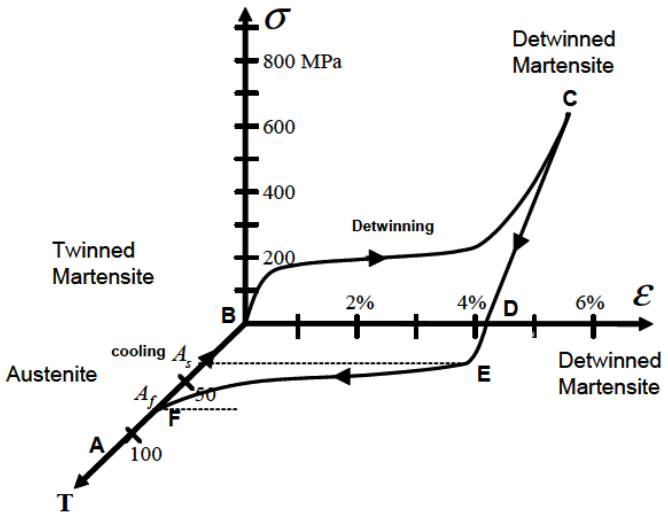


Figure 1.4: Typical shape memory effect loading path [1].

### 1.1.4 Contact Mechanics of Shape Memory Alloys

The contact behavior of SMAs is classified under inelastic contact because of the associated nonlinear constitutive behavior. This renders closed-form solutions for the stresses and displacements under normal and tangential tractions to be intractable. The majority of studies in the available literature that investigate computational contact mechanics of SMAs do not focus specifically

on the stress field and deformations that arise due to the pseudoelastic or shape memory behavior of the material under contact but rather on the force-displacement relationships during indentation (normal contact) and unloading. A summary of these works is provided and implications of the constitutive behavior under normal contact (indentation) are discussed.

In one of the earliest studies involving the contact behavior of pseudoelastic SMAs, Liu and Li [31] used FEM to study the wear behavior of interacting asperities, with one of the asperities modeled as a pseudoelastic SMA. The wear behavior was characterized by studying the accumulated plastic strain generated during the asperity on asperity interaction. A comparison study between NiTi and steel 304 was performed and results demonstrated that as the normal contact force between the asperities increased, the amount of plastic strain in the pseudoelastic NiTi asperity was significantly smaller than the accumulated plastic strain in steel 304 asperity. This was then extended to study the feasibility of improving the wear life of NiTi by reinforcing the NiTi matrix with nano TiN powder [32]. While these studies numerically demonstrate the superior wear resistance of SMAs, they do not explain the constitutive model used to simulate the pseudoelastic behavior. In a more analytical formulation, Shaw et al. [33] used the expanding spherical cavity model developed by Hill [34, 35] and later adopted by Johnson [36] for the study of conventional elastic-plastic materials, to predict the recovery ratio of SMAs undergoing the shape memory effect during nanoindentation. The theoretical recovery ratio is defined as the ratio of the thickness of the region that experiences deformation via martensitic rearrangement to the radius of the elastic-plastic boundary. While the theoretical results match fairly well with the experimentally measured recovery ratio, the model fails to account for any hardening behavior of NiTi in the transformation region. Wood and Clyne [37] used the SMA constitutive model developed by Auricchio and Taylor [38] in a finite element model to study the nanoindentation response of SMAs for both spherical and conical indenters. Results demonstrated that for the conical indenter, the region surrounding the indentation was dominated by plasticity. This was attributed to stress singularities at the cone tip. A good agreement between the model and experimental load-displacement results was obtained. For the sphere however, at temperatures above $A_f$, some pseudoelasticity in addi-

tion to plasticity was observed and the model was not able to accurately match the experimental results at these temperatures. The authors attributed this difference to the limited capability of the model to accommodate compressive work-hardening characteristics compared to tensile loading on which the model was originally developed for. A similar study was conducted by Zhang et al. [39] using a modified version of the Ivshin-Pence model [40] where a good co-relation between experimental and numerical spherical pseudoelastic indentation and recovery was observed even for spherical indenters. In another study investigating the wear resistance of SMAs, Yan [41] used the maximum contact pressure developed during spherical indentation as a metric for the wear resistance capability. A parametric study is conducted for different transformation strains and forward transformation stresses and the maximum contact pressure is tracked throughout the indentation process. The author demonstrated that the wear resistance under spherical indentation is greatest when the SMA possesses a high transformation strain and a low transformation stress. Wang et al. [42] employed a bilinear strain hardening model to capture the pseudoelastic response of SMAs under spherical indentation and compared the response with that of stainless steel. It was shown that increasing the maximum transformation strain corresponds to a smaller region of plasticity when compared to stainless steel. More recently, Maletta et al. [43] compared experimental and numerical load-displacement curves of SMAs obtain from spherical nanoindentation at loads sufficient to induce phase transformation and at temperatures above $A_f$. The numerical and experimental results demonstrated that the recovery of the indent decreased as the load increased while the recovery of the indent increased as the temperature was increased.

Most of the cited literature focused solely on the normal contact of either the pseudoelastic or shape-memory SMAs. However as pointed out in Section 1.1.1, the presence of both normal and tangential contact alters the stress distribution in the half-space and this can have important implications when predicting the sliding wear behavior of SMAs.

### 1.1.5 Wear Behavior of Shape Memory Alloys

It is well known that the wear resistance of conventional tribo-materials is mainly dependent on their mechanical properties such as hardness, toughness, and work-hardening [44]. Hardness is of particular importance to abrasion resistance, while toughness and work-hardening are responsible for the resistance to wear under impact or high stresses. Recently, shape memory alloys have emerged as a new class of tribo-materials [45]. Unlike traditional tribo- materials that owe their wear resistance to their hardness and toughness, the wear resistance of SMAs has been attributed to several factors, such as its pseudoelasticity, pseudoplasticity (shape memory effect), low yield strength compared to other tribo-materials, or a combination of these factors. In recent years, several experimental studies have demonstrated the superior wear resistance of SMAs. What follows is a brief review of the available literature aimed at identifying the various effects attributed to the wear resistance of SMAs during sliding. In one of the earliest studies, Clayton [46] conducted sliding and rolling contact fatigue tests on 55-Nitinol (55 wt.% Nickel and 45 wt.% Ti) and observed that the SMA had a significantly higher wear resistance than conventional steel for the same experimental tests. The author attributed the wear resistance to cyclic hardening of the SMA during the sliding process. Liang et al. [47] studied the wear resistance of both pseudoelastic and pseudoplastic SMAs under sliding wear, impact abrasion and erosion and found that in all three cases, recovery due to the pseudoplastic effect was more pronounced than recovery due to pseudoelasticity. Li [45] performed several tests (indentation, sliding wear, microwear, corrosion and air-jet erosion tests) on both a heat treated SMA and a cold drawn SMA and compared the wear resistance of SMAs with that of steel 304. The sliding wear test was performed on a pin on disc tribometer, with the volume loss of the pin specimen used as an indicator of wear resistance. It was shown that for the indentation and sliding wear tests, the SMA material consistently outperformed the steel specimen. In addition, at low loads, the heat-treated specimen had lower wear resistance than the as-received specimen, indicating that heat treatment can play a major role in decreasing the wear loss of pseudoelastic SMAs.

Besides heat treatment and pseudoelasticity, there is evidence that the concentration of the

alloying elements of the SMA can also inhibit wear. Lin et al. [48] demonstrated that $Ti_{49}Ni_{51}$ alloy exhibited better wear resistance than $Ti_{50}Ni_{50}$ alloy due to its higher hardness and pseudoelastic behavior. Furthermore, sliding tests revealed that wear increases with increasing load and sliding distance but decreases with increasing sliding speed. Other studies have shown that pseudoelastic recovery of SMAs is not only dependent on the applied load and heat treatment, but also depends on the geometry of the indenter [49] and the temperature of the surface during wear [50]. For instance, Qian et al. [50] performed indentation and wear tests of an SMA using a triboindenter with the temperature controlled from 22 °C to 120 °C (all above $A_f$) using a Berkovich type diamond tip. The results of the wear tests indicated that for a fixed load, the wear resistance decreased as the operating temperature increased. This phenomenon was attributed to an increase of the plastic yield stress of austenite and the phase transition stress with temperature. A similar trend was also obtained by Abedini et al. [51] for near equi-atomic NiTi alloy with composition of Ti50.3 wt%. However, these experimental tests were conducted at operating temperatures both above and below the austenite finish temperature. More recently, Yan and Liu [52] added more insight to this phenomenon by identifying two different wear modes for purely austenitic SMAs. Mode 1 occurred within the temperature range of $A_f < T < M_d$ , where $M_d$ is the maximum temperature at which stress induced martensite can occur. Within this mode, wear resistance increased with increasing temperature until the point where the contact stresses exceeded the yield strength of martensite. Mode 2 corresponds to a temperature range of $T > M_d$ where the austenitic phase loses its pseudoelasticity and the wear resistance deteriorates as the alloy follows a conventional strain-hardening behavior.

In summary, there are several experimental and material factors that have been attributed to the superior wear resistance of SMAs when compared to traditional wear resistant metals. With the aim of further improving the wear resistance of these unique alloys, the critical material parameters that affect them and means to modify them need to be further studied. With the aid of constitutive models that accurately simulate the behavior of these materials, these key material parameters that can improve the wear resistance of these materials can be identified.

## 1.2 Research Objectives and Thesis Outline

Most of the aforementioned computational studies on modeling the contact behavior of SMAs focus purely on either the pseudoelastic or pseudoelastic-plastic response of SMAs due to indentation (normal contact). The cited literature on experimental wear resistance of SMAs however, demonstrates that wear resistance is typically measured under sliding wear and not through indentation experiments. While indentation simulations provide a general overview of the complex stress fields during loading and unloading, they do not account for the evolution of these complex stress fields during forward and reverse transformations under combined normal and tangential tractions. To fill this gap, this thesis focuses on simulations that study the pseudoelastic response of SMAs under sliding contact. The pseudoelastic behavior is simulated using the phenomenological constitutive model put forward by Lagoudas et al. [53]. The sliding contact problem studied is that of an infinitely long cylinder of radius $R$ indenting a pseudoelastic semi-infinite half-space and sliding to a finite distance. This problem can be modeled in 2-D by invoking the plane strain assumption. A parametric study is then performed to study the effect of key material properties and contact definitions on the stress distribution in the half-space. The primary objectives of this research effort are stated as follows:

1. *To study the effect that phase transformation and pseudoelasticity have on the sliding contact response of shape memory alloys.*

   The cited literature indicates that pseudoelasticity contributes to the superior wear resistance of SMAs when compared to traditional tribo-materials. One possible reason is that stress induced transformation to martensite during indentation and sliding leads to a phase that has a lower modulus than the parent austenite phase and consequently leads to a decrease in the stress in the substrate. Another possible reason is that the maximum amount of recoverable strain can help relieve some of stress observed during the indentation and sliding contact process. Parametric studies investigating the effects of the difference in elastic modulus between the two phases as well as the degree of maximum recoverable transformation strain on the sliding contact response will be conducted.

2. *To study the effect that the operating temperature has on the sliding contact response of shape memory alloys.*

   Studies involving isothermal loading paths both above and below the austenite finish and start temperatures will be conducted to determine their effect on the sliding response. It is expected that complete recovery of indentation induced martensite in the substrate is achieved during the sliding process at operating temperatures above the austenite finish temperatures.

3. *To study the effect of friction on the pseudoelastic sliding contact response of a shape memory alloy half-space*

   The effect of interfacial friction between bodies in contact is an integral part of computational contact mechanics and wear prediction studies. The effect of friction on the sliding contact of a pseudoelastic half-space will be investigated by studying the stress distribution during sliding for different coefficients of friction.

The rest of this thesis is summarized as follows. Section 2 briefly introduces the constitutive model employed in the finite element simulation and outlines the key material parameters chosen for the simulation. It also describes the modeling procedure for the sliding process and assumptions made therein. The results of a parametric study studying the effects of the max transformation strain, operating temperatures and the coefficient of friction on the sliding response are presented in Section 3 and key conclusions are summarized in Section 4.

# 2. MODELING FRAMEWORK

This section provides a general overview of the SMA constitutive model as well as a description of the contact model available in the finite element software. The various contact controls employed to accurately simulate the normal and sliding contact between the indenter and the half-space are also discussed. The Hertzian normal contact and sliding contact analytical formulations are compared with analogous results obtained from FEM simulations so as to demonstrate the validity of the numerical model to be used for the pseudoelastic normal and sliding contact studies.

## 2.1 Key Assumptions

The following assumptions are used to simplify the problem

1. The cylinder and the half-space are assumed to be infinitely long such that contact problem can be reduced to a two-dimensional plane strain contact problem. Since it is not realistically possible to model an infinite body using the finite element method, it is assumed that the chosen finite dimensions of the half-space are large enough to closely approximate an analytical infinite half-space.

2. The constitutive behavior of the SMA does not account for dislocation-slip plasticity. Although in a typical sliding wear process, wear initiates due to accumulated plastic strain in the specimen, the effects of phase transformation during sliding needs to be well understood before the combined effects of phase transformation and plasticity are studied.

3. The normal and sliding contact process is simulated in an isothermal environment. Therefore, thermal variations at the contact surface as a result of frictional heat generation are not considered.

4. The normal and sliding contact process is also simulated in a quasi-static manner with the loads/displacements applied incrementally. Therefore, dynamic effects of an indenter sliding

with a particular velocity are not considered. Likewise, the material properties of the SMA do not depend on the quasi-static strain rate.

## 2.2 Shape Memory Alloy Constitutive Model

The constitutive model used in this study is based on a thermodynamic framework and what follows is a condensed description of the model. A more detailed explanation can be found in the works by Boyd and Lagoudas [54] and Lagoudas et al. [53]. The formulation is developed by first stating the total Gibbs free energy

$$G\left(\boldsymbol{\sigma}, T, \xi, \varepsilon^t\right) = -\frac{1}{2\rho}\boldsymbol{\sigma} : \boldsymbol{S} : \boldsymbol{\sigma} - \frac{1}{\rho}\boldsymbol{\sigma} : \left[\boldsymbol{\alpha}\left(T - T_0\right) + \boldsymbol{\varepsilon^t}\right] + c\left[\left(T - T_0\right) - T\ln\left(\frac{\mathrm{T}}{\mathrm{T_0}}\right)\right] - s_0 T + u_0 + \frac{1}{\rho} f\left(\xi\right) \tag{2.1}$$

where $\sigma$ is the Cauchy stress tensor, $\varepsilon^t$ is the transformation strain tensor, $\xi$ is the martensite volume fraction, $T$ is the current temperature, $T_0$ is the reference temperature, $f(\xi)$ is the transformation hardening function. $\boldsymbol{S}, \boldsymbol{\alpha}, \rho, c, s_0$ and $u_0$ are the material constants which refer for the effective compliance tensor, effective thermal expansion tensor, density, effective specific heat, effective entropy at reference state and effective specific internal energy at reference state [54]. By the rule of mixtures, these material constants are defined as follows:

$$\begin{aligned}
\boldsymbol{S}(\xi) =& \boldsymbol{S^A} + \xi\left(\boldsymbol{S^M} - \boldsymbol{S^A}\right) = \boldsymbol{S^A} + \xi\Delta S \\
\boldsymbol{\alpha}(\xi) =& \boldsymbol{\alpha^A} + \xi\left(\boldsymbol{\alpha^M} - \boldsymbol{\alpha^A}\right) = \boldsymbol{\alpha^A} + \xi\Delta\alpha \\
c(\xi) =& c^A + \xi\left(c^M - c^A\right) = c^A + \xi\Delta c \\
s_0(\xi) =& s_0^A + \xi\left(s_0^M - s_0^A\right) = s_0^A + \xi\Delta s_0 \\
u_0(\xi) =& u_0^A + \xi\left(u_0^M - u_0^A\right) = u_0^A + \xi\Delta u_0
\end{aligned} \tag{2.2}$$

where the superscripts $A$ and $M$ refer to the austenite and the martensite phases, respectively.

The total strain equation is the sum of the elastic, thermoelastic and transformation strain and

is given by

$$\boldsymbol{\varepsilon} = -\rho\frac{\partial G}{\partial \sigma} = \boldsymbol{S} : \boldsymbol{\sigma} + \boldsymbol{\alpha}\left(T - T_0\right) + \boldsymbol{\varepsilon^t} \tag{2.3}$$

where $\boldsymbol{\varepsilon}$ is the strain tensor and $\boldsymbol{\varepsilon^t}$ is the transformation strain tensor. In this study, it is assumed that the thermoelastic strain is not that significant.

The martensite volume fraction $\xi$ is treated as an internal state variable and is related to the other internal state variable $\varepsilon^t$. The evolution of $\xi$ is described by

$$\dot{\boldsymbol{\varepsilon}}^{\boldsymbol{t}} = \boldsymbol{\Lambda}\dot{\boldsymbol{\xi}} \tag{2.4}$$

where $\boldsymbol{\Lambda}$ is the transformation tensor that determines the transformation strain direction. The transformation tensor $\boldsymbol{\Lambda}$ for proportional loading case (e.g., uniaxial loading) is expressed by two different forms as follows:

$$\boldsymbol{\Lambda} = \begin{cases} \Lambda^{fwd} = \frac{3}{2}H^{cur}\frac{\boldsymbol{\sigma'}}{\bar{\sigma}}; & \dot{\xi} > 0, \\ \Lambda^{rev} = \frac{\boldsymbol{\varepsilon}^{t-r}}{\xi}; & \dot{\xi} < 0. \end{cases} \tag{2.5}$$

where $H^{cur}$ is the uniaxial transformation strain for full transformation, $\boldsymbol{\varepsilon}^{t-r}$ is the transformation strain at reverse transformation, $\boldsymbol{\sigma'}$ is the deviatoric component of the stress tensor and $\bar{\sigma}$ is the effective stress defined using the von Mises criterion as :

$$\bar{\sigma} = \sqrt{\frac{3}{2}\boldsymbol{\sigma'} : \boldsymbol{\sigma'}} \tag{2.6}$$

$H^{cur}$ is defined as a decaying exponential function of the applied load and is given as

$$H^{cur}\left(\bar{\sigma}\right) = \begin{cases} H^{min}; & \bar{\sigma} \leq \bar{\sigma}_{crit}, \\ H^{min} + \left(H^{max} - H^{min}\right)\left(1 - \mathrm{e}^{-k(\bar{\sigma} - \bar{\sigma}_{crit})}\right); & \bar{\sigma} \geq \bar{\sigma}_{crit}. \end{cases} \tag{2.7}$$

where $H^{min}$ gives the transformation strain attained when no external loads are applied to the material, $H^{max}$ is the ultimate potentially attainable transformation strain under uniaxial loading,

and $\bar{\sigma}_{crit}$ is the minimum equivalent stress required to generate transformation strains higher than $H^{min}$. The $k$ parameter controls the rate at which $H^{cur}$ increases from $H^{min}$ to $H^{max}$ and is typically chosen based on experimental calibration.

During transformation, the thermodynamic driving forces $\pi$ must balance the critical thermodynamic driving force required for transformation, $Y$. This balance is termed the transformation yield surface $\Phi$, which has the condition that during transformation, there should be maximum dissipation, analogous to $J_2$ plasticity theory,

The thermodynamic force $\pi$ is expressed in conjunction with the martensite volume fraction $\xi$ as follows:

$$\begin{aligned}\pi\left(\sigma, T, \xi\right) =& \boldsymbol{\sigma} : \boldsymbol{\Lambda} + \frac{1}{2}\boldsymbol{\sigma} : \Delta\boldsymbol{S} : \boldsymbol{\sigma} + \boldsymbol{\sigma} : \Delta\boldsymbol{\alpha}\left(T - T_0\right) \\ &+ \rho\Delta c\left[\left(T - T_0\right) - T\ln\left(\frac{T}{T_0}\right)\right] - \rho\Delta s_0 - \rho\Delta u_0 - \frac{\partial f}{\partial \xi}\end{aligned} \tag{2.8}$$

and the transformation yield surface $\Phi$ is defined as a function of the thermodynamic force $\pi$ as

$$\Phi = \begin{cases} \pi - Y; & \dot{\xi} > 0, \\ -\pi - Y; & \dot{\xi} < 0. \end{cases} \tag{2.9}$$

Since $\pi$ must balance $Y$ during both forward and reverse transformation, this essentially renders $\Phi = 0$ during this process.

To ensure a smooth transition from the elastic state to the transformation response, the hardening function $f(\xi)$ is defined using a power law in terms of $\xi$ with real exponents.

$$f\left(\xi\right) = \begin{cases} \frac{1}{2}a_1\left[1 + \xi^{n_1} - \left(1 - \xi\right)^{n_2}\right] + a_3; & \dot{\xi} > 0, \\ \frac{1}{2}a_2\left[1 + \xi^{n_3} - \left(1 - \xi\right)^{n_4}\right] + a_3; & \dot{\xi} < 0. \end{cases} \tag{2.10}$$

where $a_i (i = 1, 2, 3)$ are coefficients that assume real values, and $n_i (i = 1, 2, 3, 4)$ are exponents which assume real numbers $0 < n_i \leq 1$.

The constitutive equations described above yield material and phase transformation parame-

ters that are eventually used to calibrate the model so as to match experimental results. These parameters can be broken into three categories

- Thermoelastic Parameters

  $E_A, E_M, \nu_A, \nu_M, \alpha_A, \alpha_M$

  where $E$ is the elastic modulus, $\nu$ the Poisson ratio, $\alpha$ the thermal expansion coefficient and the subscripts $A$ and $M$ represent the austenite and martensite phase. The elastic constants are measured from isothermal stress-strain curves in each phase.

- Transformation strain Parameters

  $H^{min}, H^{max}, \bar{\sigma}_{crit}, k$

  are defined above and are typically calibrated directly from isobaric experimental tests under thermal variations where the value of $k$ in particular is empirically chosen by fitting the $H^{cur}$ function to the data.

- Phase Transformation Parameters

  $M_s, M_f, A_s, A_f, C_M, C_A, n_1, n_2, n_3, n_4$

  where $M_s, M_f, A_s, A_f$ are the martensite start, martensite finish, austenite start, austenite finish temperatures, $C_M, C_A$ are the slopes of the phase-temperature diagram, $n_i (i = 1, 2, 3, 4)$ are the smoothening coefficients.

These constitutive equations have been implemented into a user material sub-routine in the finite element software ABAQUS.

## 2.3 Contact Model

Contact between the cylinder and the half-space is defined in the finite element software using a master-slave contact pair approach. The cylindrical rigid body is specified as the master surface and the surface of the refined mesh of the half-space that is to be in contact with the rigid body throughout the simulation is specified as the slave surface. Prior to the indentation process, contact between the indenter and the half-space needs to be detected. This is enforced via the so called "hard" contact pressure - overclosure" relationship. Hard contact implies that the surfaces transmit no normal traction unless the nodes of the slave surface make contact with the master surface and that zero penetration of the master surface beyond the nodes of slave surface in the contact region is allowed [55]. At the instance of sliding between the contact pairs, this study considers the effect of both a friction and a frictionless interaction. When friction is enabled, the Coulomb friction model is employed to relate the maximum allowable frictional (shear) stress across an interface to the contact pressure between the contacting bodies by specifying a value for the coefficient of friction $\mu$. In this friction model, as long as lateral surface traction $q(x)$ is less than the product of the specified friction coefficient $\mu$ and the contact pressure $p(x)$ , the contacting interfaces will stick. Gross slip occurs when $q(x)$ in the whole region increases beyond this limit.

ABAQUS offers different contact formulations that govern the relative motion between the contact pair (indenter and half-space) during the sliding process, namely the small and finite sliding contact formulations. In this study, the finite sliding tracking option instead of the small sliding tracking option because of the large displacement controlled sliding distance considered in this study. The small-sliding formulation assumes that throughout the sliding process, even if the surfaces undergo large deformation/rotations, a slave node on the surface of the half-space will always interact with the same local area of the indenter it was originally in contact with. This behavior differs from finite-sliding contact problems, where the contact area changes due to large sliding.

ABAQUS/Standard applies conditional constraints at various locations on each surface to simulate contact conditions and accurately measure the contact area and contact pressure. ABAQUS/Standard

offers two contact discretization options: a traditional node-to-surface discretization and a true surface-to-surface discretization. The current study employs the node-to-surface discretization approach since node-to-surface contact discretization tends to be less costly per iteration than surface-to-surface contact discretization (because surface-to-surface contact discretization generally involves more nodes per constraint). For the case when the slave surface consists of a node-based surface, the contact pressure is equal to the normal contact force divided by the cross-sectional area at the contact node.

## 2.4 Finite Element Model

This study involves a plane strain assumption wherein a rigid cylinder of radius $R = 0.01$ mm indents and slides along a pseudoelastic semi-infinite half-space. The rigid cylinder and the half-space are assumed to be infinitely long in the direction perpendicular to sliding which simplifies the analysis to a 2D finite element problem as shown in Figure 2.1.

The assembly consists of the cylinder modeled as an analytical rigid body, the geometry of which is defined by equations, rather than nodes. The half-space is modeled as a deformable body. The subsequent analysis is performed by utilizing the implicit solver of the FEM package. The half space is modeled using 4-node plane strain linear elements with reduced integration (CPE4R). The reduced integration scheme is preferred to a full integration scheme because it results in a better approximation for analyses of nonlinear material behavior [56, 57]. To achieve accurate results, a high mesh density is specified in the vicinity of the contact zone, while the mesh gets gradually coarser farther away from the contact zone. This is accomplished by partitioning the half-space appropriately, with the partition size getting progressively larger away from the contact zone. The local mesh seed size in and around the contact zone is determined from a mesh density convergence study. Further details as to the size of the domain, element size and mesh density are included in the mesh convergence study outlined in Section 2.5 Mesh Domain Convergence.

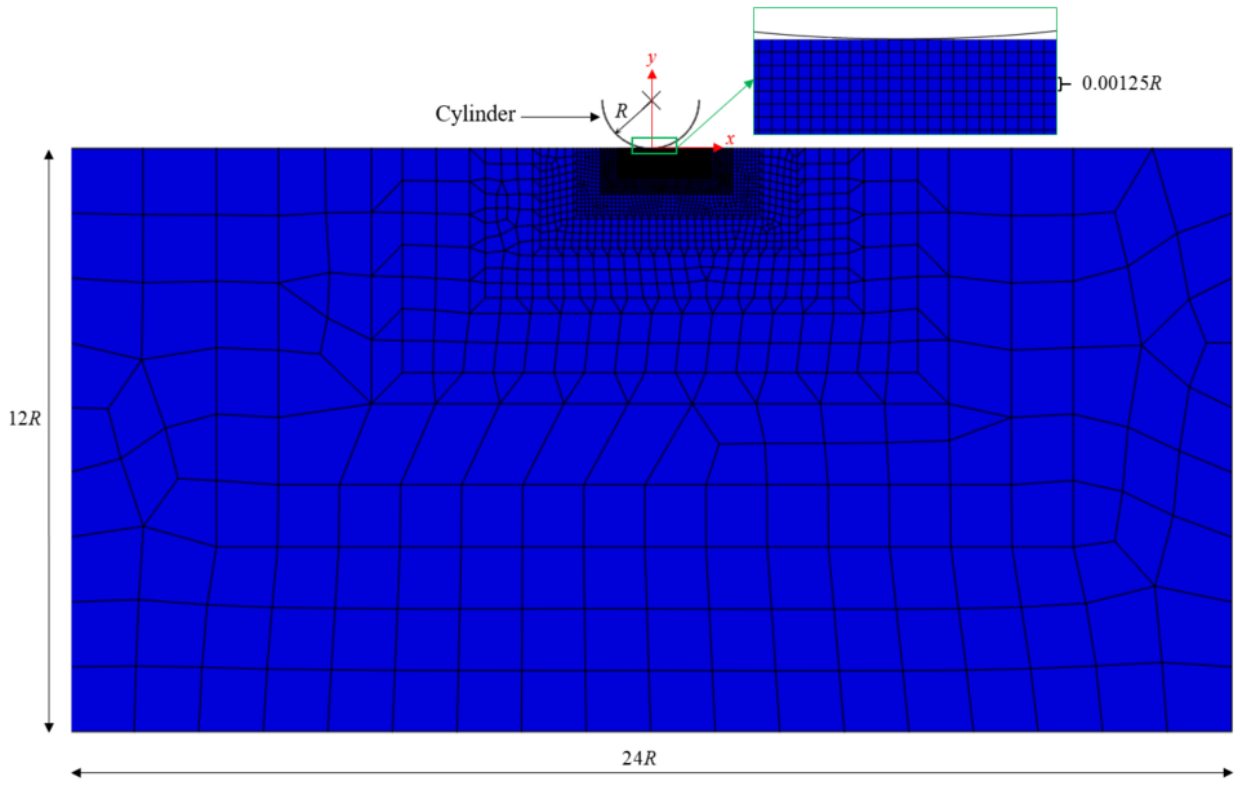


Figure 2.1: Two dimensional pseudoelastic half-space in contact with a rigid cylinder of radius $R$ (lower half shown).

The temperature of the simulation is then specified under the Predefined Field Option in ABAQUS. All simulations are performed in an isothermal environment, i.e., temperature effects that may occur due to frictional sliding are ignored and the material properties of the SMA are assumed to be at a specified operating temperature. Furthermore, the material response of the shape memory alloy due to sliding remains in the elastic regime of both martensite and austenite, i.e., no dislocation plasticity is considered for the pseudoelastic case.

Sliding contact is enforced via a displacement controlled approach in two steps. In the first step, a normal displacement is incrementally applied in the $-y$ direction at the master node/reference point of the rigid cylinder, while constraining the movement in the $+x$ direction and rotation about the out of plane axis to be zero. The value of the normal displacement is appropriately chosen

so as to initiate stress induced martensite in the indentation step. In the second step, the cylinder slides horizontally by specifying an incremental horizontal displacement in the $+x$ direction while maintaining the normal displacement specified in the previous step. In a similar manner to the first step, the rotation about the out of plane axis is constrained to be zero to prevent the indenter from rolling during the sliding step. The initial position of the rigid body is specified at the plane of symmetry $x = 0$ as shown in Figure 2.1.

## 2.5 Mesh Domain Convergence

In this section, the appropriate size of the domain of the half-space is determined so as to accurately model a semi-infinite half-space behavior. This is established by undertaking a domain convergence study in which the dimensions of the half-space are proportionately increased until convergent results are obtained. This is also performed to ensure that the size of the half-space is large enough so that the boundary conditions specified at the fringes of the domain do not interfere with the results near the contact region. For the domain convergence study, the half space is assumed to be elastic with a modulus of elasticity $E$=55 GPa and a Poissons ratio $\nu$=0.3. The rigid cylinder has a radius $R$=0.01 mm while the dimensions of the half-space are increased while maintain the same aspect ratio of the half-space, i.e., the length of the half-space is always twice that of the height of the half-space. The height of the half-space is then increased from $2R$ to $14R$ and the contact pressure distribution due to an applied normal displacement of $\Delta y = 0.008R$ is calculated and used as a metric to determine if convergent results are achieved.

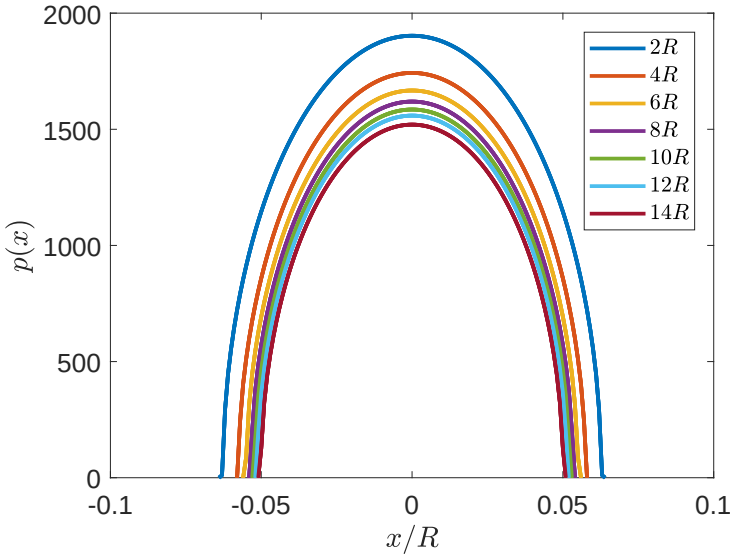


Figure 2.2: Half-Space Domain convergence study where the height $H$ of the domain is varied from $2R - 14R$, the length $L = 2H$.

Figure 2.2 demonstrates that the contact pressure gradually decreases as the size of the domain increases until the results for considerably large domains $12R - 14R$ are comparable. The fact that the contact pressure decreases as the size of the domain increases suggests a reduced effect of the boundary conditions applied on the edges of the half-space. Based on this result, the height of the domain is chosen as $12R$ and the length of the domain chosen as $24R$.

A separate study is performed to determine the appropriate size of the elements in the contact region so as to achieve an accurate mesh discretization in the contact region. The size of the each element in the contact region is varied from $0.01R$ to $0.00085R$ and the contact pressure distribution obtained due to normal contact for the similar indentation depth of $\Delta y/R$=0.008 is studied. The same elastic properties as in the previous convergence study are used. Figure 2.3 demonstrates the contact pressure distribution for these different element sizes. While the maximum contact pressure remains approximately the same as the element size decreases, the size of the contact region gradually shrinks suggesting that a larger element size over predicts the region of contact. Based on this study, the final element size for the linear quadrilateral element in the

contact region is selected as $000125R$. The final model has 96763 nodes and 96523 elements.

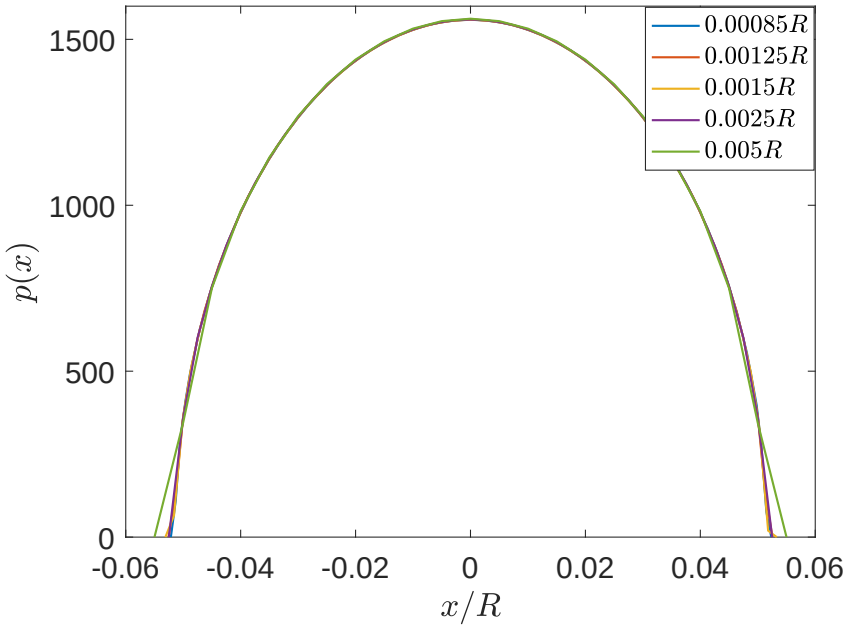


Figure 2.3: Contact region element size convergence study.

## 2.6 Model Validation

The contact formulation and definitions in the finite element model (node to surface contact formulation) and the mesh convergence findings are compared and validated against solutions to established contact mechanics problems. Three separate validation studies are performed to determine the accuracy of finite element model. In the first and second validation studies, the numerical interior stress fields in the half-space are compared with the elastic closed form expressions for the interior stress fields available in the literature. In the third validation study, the analytical expressions for the critical distributed force required to initiate yield are modified to derive the critical distributed force required to initiate phase transformation in the half-space and these results are compared with the numerical force obtained using the FEM model.

### 2.6.1 Normal Contact

The first validation study investigates the elastic normal contact problem of a cylinder of radius $R_1$ and elastic material properties $E_1, \nu_1$ in normal contact with another cylinder of radius $R_2$ and elastic material properties $E_2, \nu_2$, where $E_i, \nu_i$ are the elastic modulus and Poisson ratio respectively. For an applied load $F$, the normal traction or contact pressure distribution according to Hertz is given by

$$p(x) = p_0 \sqrt{1 - \left(\frac{x}{a}\right)^2}, \quad -a < x < a \tag{2.11}$$

where $a$ is the contact radius, $p_0$ is the maximum contact pressure, and $x$ is the spatial dimension in the contact region defined by $a$. Outside of this region, the contact pressure is effectively zero. The contact radius is a function of the applied load, combined elastic properties of the two materials and the radii of the two cylinders and is given by

$$a = \sqrt{\frac{4FR^*}{\pi E^*}} \tag{2.12}$$

and the maximum contact pressure $p_0$ is also a function of the applied load, elastic properties and radii of the two cylinders

$$p_0 = \sqrt{\frac{FE^*}{\pi R^*}} \tag{2.13}$$

where $E^*$ and $R^*$ are the effective elastic modulii and effective radius and are expressed as

$$\begin{aligned} E^* &= \left(\frac{1-\nu_1^2}{E_1} + \frac{1-\nu_2^2}{E_2}\right)^{-1} \\ R^* &= \left(\frac{1}{R_1} + \frac{1}{R_2}\right)^{-1} \end{aligned} \tag{2.14}$$

To model a half-space, the radius of one of the cylinders $R_2$ is set to $\infty$. To model the rigid cylinder, the elastic modulus of other cylinder, $E_1$ is also set to $\infty$. The resulting problem can be visualized in Figure 2.4

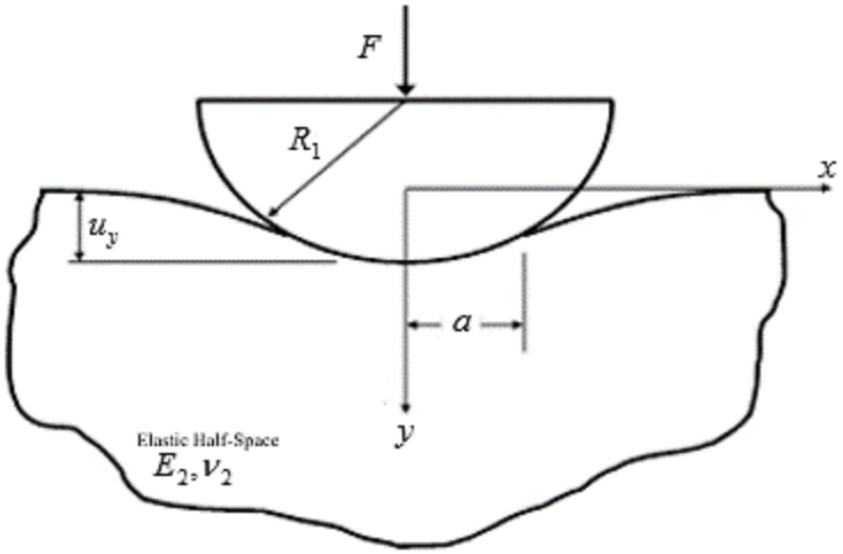


Figure 2.4: Normal contact of a rigid cylinder on an elastic half-space.

For the finite element model, instead of using a displacement control approach adopted in the model domain and mesh convergence study, a load control approach is used. A load equal to $F$=1.25 N/mm is used in the simulations and the analytical model. The elastic properties of the half-space selected are $E_2$=55 GPa, $\nu_2 = 0.3$ which are the same as the elastic properties of austenite that will be chosen for the parametric study to be discussed later. The radius of the indenter $R$ is selected as 0.01 mm. The load is applied at the master node/reference point of the rigid cylinder. Figure 2.5 shows the results of the contact pressure distribution for the Hertzian contact problem. An excellent correlation between the two approaches is obtained.

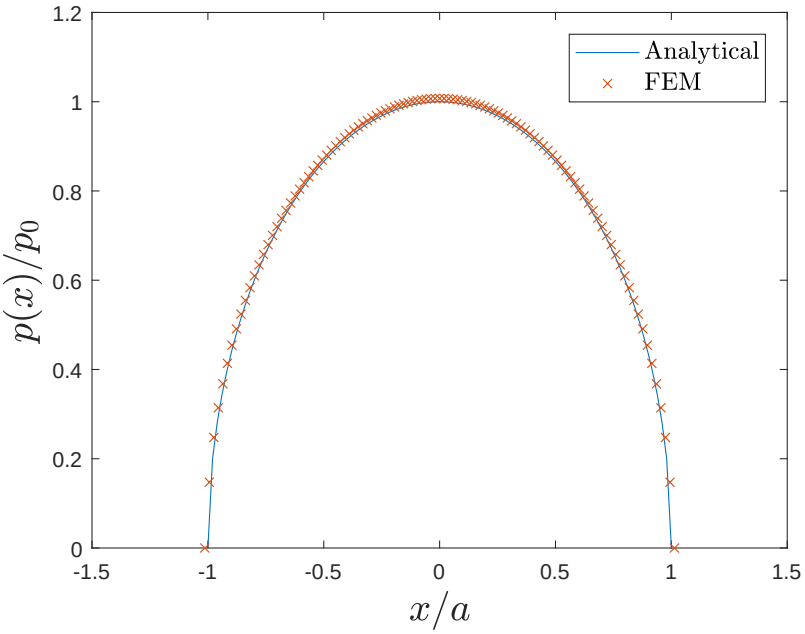


Figure 2.5: Comparison of contact pressure distribution (Analytical vs. FEM).

The solution for stresses $\sigma_{xx}, \sigma_{yy}$ and $\tau_{xy}$ in the elastic half-space are given by Johnson [4]. These stresses along the axis of symmetry of the indenter $x = 0$ and in the half-space (Figure 2.4) are expressed explicitly as

$$\begin{aligned} \sigma_{xx} &= -\frac{p_0}{a}\left(\left(a^2+2y^2\right)\left(a^2+y^2\right)^{-1/2} - 2y\right) \\ \sigma_{yy} &= -\frac{p_0}{a}\left(a^2+y^2\right)^{-1/2} \end{aligned} \tag{2.15}$$

A comparison of the stresses using FEM and their analytical equivalent is shown in Figure 2.6. The satisfactory overlap of the two results further confirms that hard contact pressure overclosure relationship specified for normal contact in ABAQUS accurately simulates the normal indentation process.

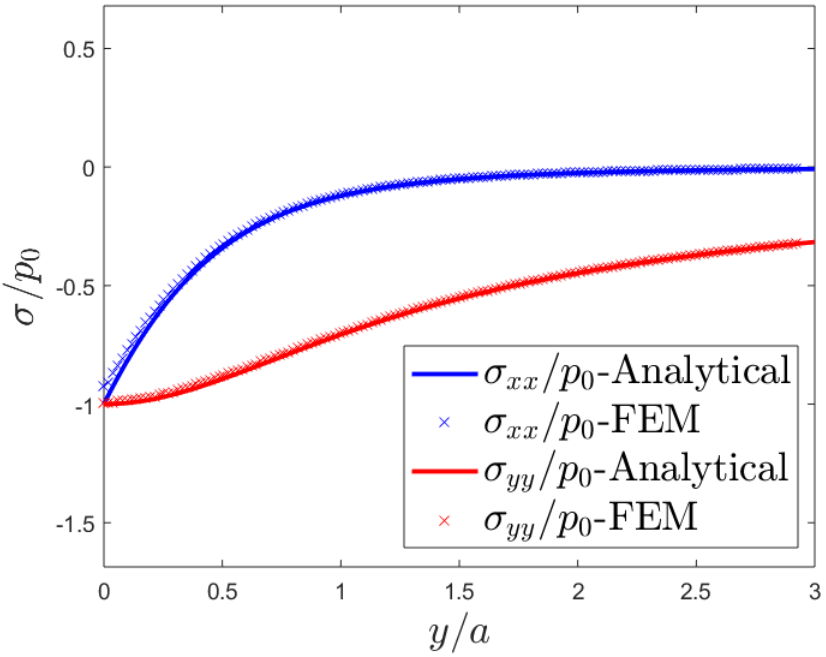


Figure 2.6: Comparison of sub-surface stress distribution in the half-space along $x/a = 0$ ($F = 1.25$ N/mm, $\mu = 0$).

### 2.6.2 Sliding Contact

In the second validation study, the stresses in the half-space due to sliding contact are studied. The analytical solution for the stresses developed due to sliding contact on an elastic half-space are provided by Smith and Liu [10] and are reproduced below

$$\begin{aligned}
\sigma_{xx} &= -\frac{p_0}{\pi}\left\{\left(a^2+2x^2+2y^2\right)\frac{y}{a}\bar{\psi} - 2\pi\frac{z}{a} - 3xy\psi \right. \\
&\qquad \left. + \mu\left[\left(2x^2-2a^2-3y^2\right)\psi + 2\pi\frac{x}{a} + 2\left(a^2-x^2-y^2\right)\frac{x}{a}\bar{\psi}\right]\right\} \\
\sigma_{yy} &= -\frac{p_0}{\pi}y\left[a\bar{\psi} - x\psi + \mu y\psi\right] \\
\tau_{xy} &= -\frac{p_0}{\pi}\left\{y^2\psi + \mu\left[\left(a^2+2x^2+2y^2\right)\frac{y}{a}\bar{\psi} - 2\pi\frac{y}{a} - 3xy\psi\right]\right\}
\end{aligned} \tag{2.16}$$

where

$$a = \sqrt{\frac{2F\Delta}{\pi}}, \quad \Delta = \frac{2R^*}{E^*}, \quad p_0 = \frac{2F}{\pi a} \tag{2.17}$$

$R^*$ and $E^*$ are the effective radius and elastic modulus of the two bodies in contact and have been defined in Eqn. 2.14, $\mu$ is the coefficient of friction, $\bar{\psi}$ and $\psi$ are functions that are dependent on the geometry of domain of the half-space.

Simulating the sliding contact problem in the finite element model requires an additional analysis step to the normal contact problem. In this step, both the normal and the tangential distributed loads are added. A normal force $F = 1.25$ N/mm is used in the simulation and the tangential load $Q = \mu F$, where $\mu$ is chosen to be 0.15. The same elastic properties of the half-space that were specified in the normal contact validation have been employed here.

The finite element and analytical stress distributions along the axis of symmetry $x = 0$ and at an arbitrary distance $x = 0.9354a$ from the axis of symmetry are compared in Figure 2.7. Near the surface of the half-space ($y = 0$), there is some slight discrepancy in the FEM results. This is likely due to a combination of the FEM results being interpolated form the integration points of the linear elements employed as well as the slight elastic slip tolerance in the friction model. Nevertheless, the general trends are the same.

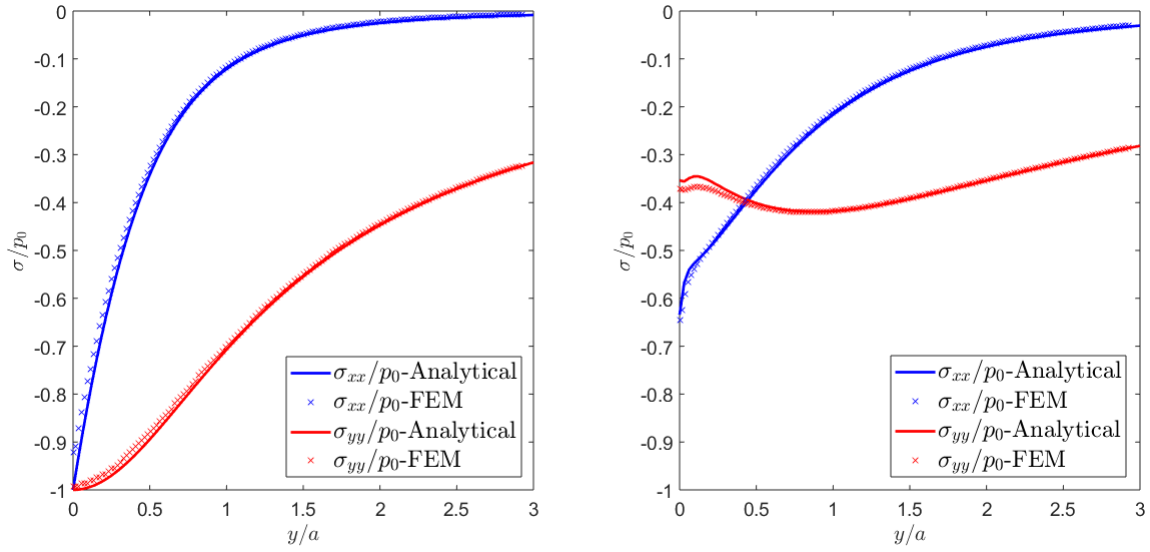


Figure 2.7: Comparison of sub-surface stress distribution in the half-space along left($x = 0$) and right ($x = 0.9354a$),($F = 1.25$N/mm, $\mu = 0.15$).

### 2.6.3 Onset of Phase Transformation

Since the SMA half-space is initially in the austenite phase, indentation at a certain load will trigger phase transformation. From principles of classical contact mechanics, it is known that for parabolic shaped indenters (spheres/cylinders), the maximum von Mises stress in the half-space exists not at the contact region but instead at some point in the half-space that is directly below the center of the indenter.

Johnson [4] provides an analytical expression for the critical force needed to be applied on the cylindrical indenter so as to initiate plastic yield in the half-space. This equation is calculated based on the von Mises yield criterion and is given by:

$$F^Y_{crit} = \frac{\pi R}{E^*}(1.79\sigma_Y)^2 \tag{2.18}$$

where$R$ is the radius of the cylinder, $E^*$ is the reduced modulus defined above and $\sigma_Y$ is the yield strength of the material. The constant 1.79 is a parameter that varies based on the yield

criterion used and also depends on the Poisson ratio of the half-space as pointed out by Green [14]. In this case, the von Mises yield criterion is employed for purposes of comparison. A similar form of equation 2.18 can be used to determine the critical force per unit length required to initiate phase transformation since the current SMA constitutive model uses the von Mises $J_2$ plasticity theory to determine the onset of phase transformation. If the initial phase of the SMA is austenite, then the critical stress required to initiate transformation to martensite $\sigma_{Ms}$ is given by

$$\sigma_{Ms} = C_M(T - M_s) \tag{2.19}$$

where $C_M$ is the slope of the stress-temperature relationship corresponding to the martensite phase in the phase diagram, $M_s$ is the martensite start temperature of the SMA at zero load and $T$ is the temperature of the isothermal loading path. Substituting the critical transformation stress in equation 2.19 for the yield stress in equation 2.18, an expression for the critical normal load to initiate phase transformation $F^T_{crit}$ is then given by

$$F^T_{crit} = \frac{\pi R}{E^*}[1.79C_M(T - M_s)]^2 \tag{2.20}$$

Using the finite element contact model described earlier but now with the constitutive model parameters outlined in Table 1, the numerical critical force required to initiate transformation in the half-space is compared with the analytical form in equation 2.20. A normal load of $F = 1.25$ N/mm is specified as the line load and the cylinder is assumed to have a radius $R = 0.01$ mm. The normal force is applied incrementally and the contact force corresponding to increment when the martensite volume fraction $\xi$ of an element in the half-space transitions from 0 to a non-zero value is recorded. This is repeated for several different temperatures $T$ and the result of the comparison between the analytical and numerical solutions are shown in Figure 2.8.

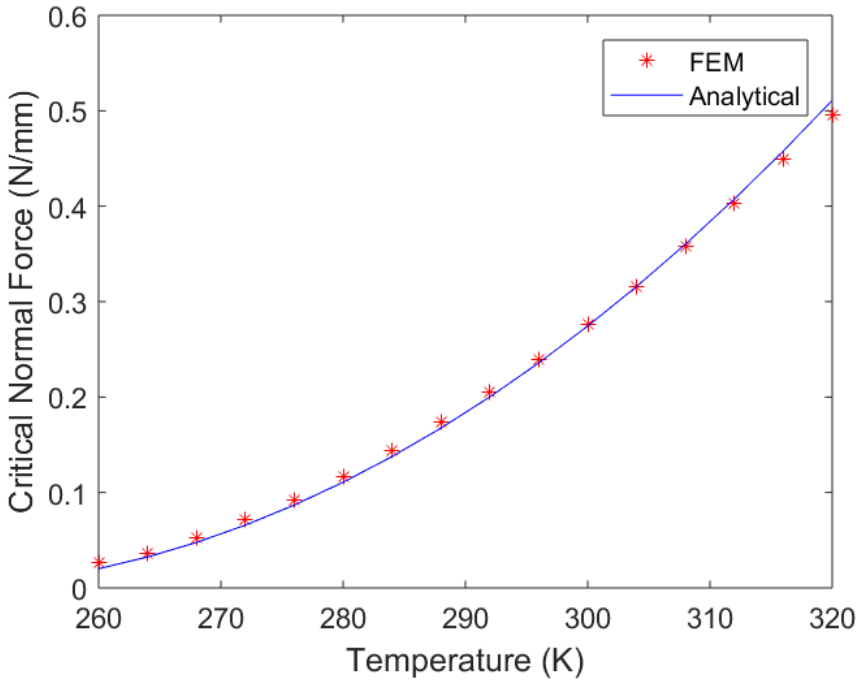


Figure 2.8: Comparison between FEM and analytical predictions for the critical normal distributed force to initiate transformation in the half-space for a range of temperatures.

Figure 2.8 demonstrates that a good prediction using the two approaches is achieved, further validating the FEM model and the analytical prediction. The critical normal force increases with increasing temperature and is a result of the increase in the critical stress required for forward transformation to initiate. Consequently, if the specified load on the indenter is below the threshold limit predicted by equation 2.20, then phase transformation does not initiates and the half-space deforms elastically in the austenitic phase. In the parametric study to follow, a displacement controlled approach is used instead of the load controlled approach used in the model validation section and the displacement input is applied in a manner that phase transformation occurs in every simulation. The effects of phase transformation and ensuing stress redistribution in the half-space are compared with the case when no phase transformation is present (i.e. when the half-space deforms elastically in the austenitic phase).

# 3. PARAMETRIC STUDY

In the following parametric study, the SMA model outlined in Section 2.2 is employed in different simulation studies wherein specific parameters unique to SMAs are varied and their effects on the sub-surface stresses and contact pressure distribution during sliding are analyzed. In the first simulation study, the operating temperature of the simulation is varied at temperatures above $A_f$ , below $A_f$ and below $A_s$. In the second simulation study, the maximum transformation strain $H^{max}$ is varied from $1\%$ to $4\%$. The results are then compared to the completely elastic case (i.e. when $H^{max}$ is $0\%$). In the third simulation study, the elastic modulus of martensite is varied to study the effect of elastic properties of the stress induced phase on the response of the pseudoelastic half-space. In the final simulation study, the interfacial coefficient of friction is varied to compare the behavior of well lubricated and dry sliding of pseudoelastic SMAs. In all simulations, it is assumed that the SMA is initially in the austenitic phase.

The radius of the cylinder $R$=0.01 mm, the half-space dimension are the same as those obtained using the model domain convergence study and has a length equal to $24R$ and height equivalent to $12R$. With the exception of the simulation study that focuses on the effect of the coefficient of friction on the sliding response, the interface between the cylinder and the half-space in the rest of the simulation studies is assumed to be frictionless. In the first analysis step, an incremental normal displacement $\Delta y$ is specified in the $-y$ direction, with each increment being equivalent to $0.01\Delta y$. In the second sliding step, a tangential displacement $\Delta x$ is specified in the $+x$ direction in increments of $3.33 \times 10^{-4}$ of the total specified tangential displacement. All simulations are performed on a computer with an Intel i7-7700k processor and 32 GB RAM. Simulation time for both analysis steps was about 2.5 hours when the coefficient of friction was set to zero and about 5 hours when it was non-zero, due to the contact tracking algorithm employed.

The relevant model parameters chosen for these simulations are listed in Table 3.1.

Table 3.1: Relevant Model Parameters.

| Parameter | Value |
|---|---|
| $E_A$ | 55 MPa |
| $E_M$ | 46 MPa |
| $\nu_M = \nu_A$ | 0.3 |
| $A_f$ | 280 °K |
| $A_s$ | 270 °K |
| $M_s$ | 245 °K |
| $M_f$ | 230 °K |
| $C_A = C_M$ | 7.4 MPa/°K |
| $\alpha_A = \alpha_M$ | 0 |
| $H^{min}$ | 0 |
| $H^{max}$ | 1%-4% |
| $k_t$ | 0.00752 $\text{MPa}^{-1}$ |
| $\bar{\sigma}_{crit}$ | 8 MPa |
| $n_1 = n_2 = n_3 = n_4$ | 0.6 |

## 3.1 Effect of Temperature

This section considers the effect of the temperature on the sliding contact response. Experimental results [50,51,58] have demonstrated that the wear behavior of SMAs changes based on the operating temperature. The constitutive model is employed to provide an insight into the evolution of the stress field in the half-space at temperatures both above and below $A_f$.

The constitutive response of a single finite element at these different temperatures is first shown in Figure 3.1. At temperatures above $A_f$ a complete recovery of austenite is achieved upon unloading. At temperatures below $A_f$ , some irrecoverable strain is observed with no recovery at temperatures below $A_s$ and the SMA behaves like an elastic-plastic material. It is also observed

that as the temperature decreases, so does the critical transformation stress needed to induce a phase transformation. $\sigma_{T1}, \sigma_{T2}$ and $\sigma_{T3}$ represent the critical transformation stresses from austenite to martensite at these different temperatures.

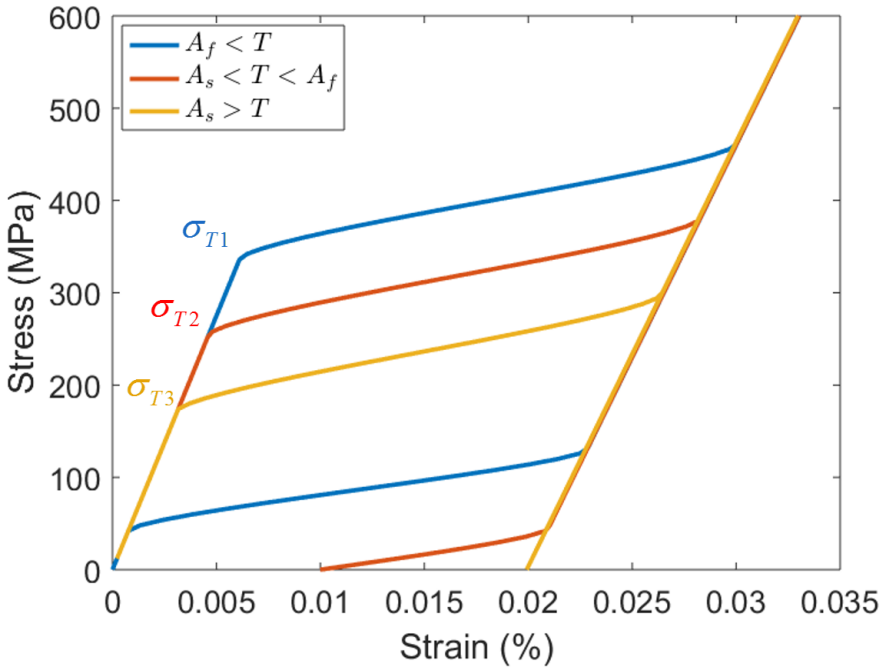


Figure 3.1: SMA constitutive response at different temperatures.

In the finite element sliding simulation, the cylinder is initially at $x = 0$ and indents the half-space to a depth of $\Delta y = 0.005R$ which is sufficient to induce phase transformation. This is followed by maintaining the same indentation depth and then sliding to a distance of $\Delta x = 0.3R$. This sliding distance is chosen so as to attain a steady state stress distribution that is unaffected by the initial indentation. It is chosen by studying the distributed normal and tangential reaction forces at the cylinder master node/reference point throughout the sliding process. The evolution of the normal and tangential loads at the different isothermal loading paths considered is demonstrated in Figure 3.2 and is compared with results of a cylinder of the same radius in sliding contact with an

elastic half-space ($E = E_A = 55$ GPa, $\nu = 0.3$) to illustrate the difference between pseudoelastic and elastic sliding contact.

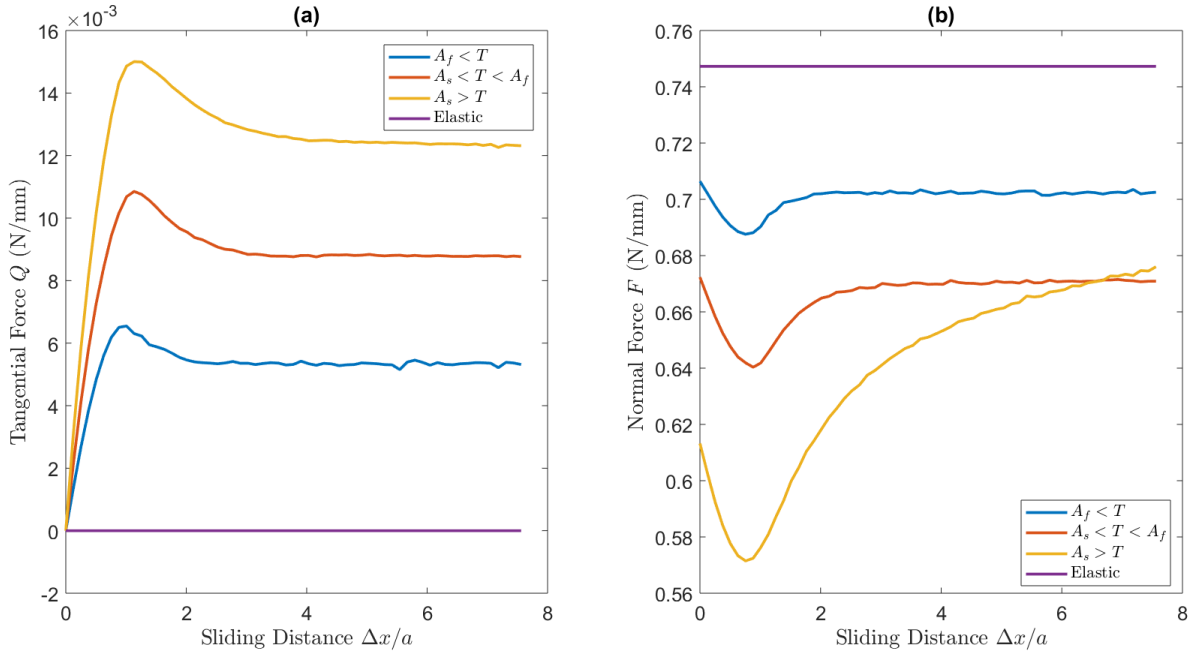


Figure 3.2: Reaction forces on the indenter at different isothermal loading paths throughout the frictionless sliding process (a) tangential distributed force (b) normal distributed force.

For an elastic material in frictionless sliding contact, the tangential force $Q$ experienced by the cylinder due to the applied normal and tangential displacement is close to zero and is likely indicative of the low indentation depth specified. This is not the case for the pseudoelastic half-space as shown in Figure 3.2 (a), where $Q$ is non-zero. At the initial stages of sliding, there is a steady climb in the tangential force in the direction of sliding as the cylinder is pushed into the depression created during the initial indentation. As the temperature of each isothermal loading path decreases, there is a proportional increase in the tangential force experienced by the indenter, thereby demonstrating the temperature dependent sliding behavior of the material. Eventually, the tangential fore reaches a steady state, however, it is observed that the sliding distance required to

reach steady state increases with the decrease in temperature. For instance, the steady state sliding distance when $A_s > T$ is achieved when the sliding distance $\Delta x$ is nearly 4 times the elastic Hertzian contact radius $a$, whereas the steady state sliding distance $\Delta x$ is $2.5a$ when $T > A_f$.

The normal force decreases during sliding and then increases until it reaches a steady state. This is observed for all simulations involving the SMA constitutive model, except for the case when $A_s > T$, where after a certain sliding distance, the normal force experienced by the indenter continues to rise and does not reach a steady state. This disparity is caused by the progressive build-up of residual stresses underneath the indenter during sliding as will be shown in the succeeding paragraphs. For the other isothermal loading paths, the normal force also decreases during the initial sliding process before eventually increasing and reaching a steady normal force that is slightly lower than the normal force at the start of sliding.

Figure 3.3 depicts the von Mises stress distribution $\sigma_{VM}$ and corresponding martensite volume fraction $\xi$ in a region of the half-space and at different stages of the sliding process. The specified temperature is $T$=285 K, which is just above the $A_f$ listed in Table 3.1. The von Mises stress in the pseudoelastic half-space is normalized by the maximum von Mises stress generated in an elastic half-space $\sigma^{max}_{VM,El}$ for the same indentation problem. The chosen spatial dimensions of the half-space are normalized by the analytical Hertzian contact radius $a$ generated due to a rigid indenter indenting an elastic half-space. The elastic half-space has the same modulus and Poisson ratio as the SMA in its austenitic phase.

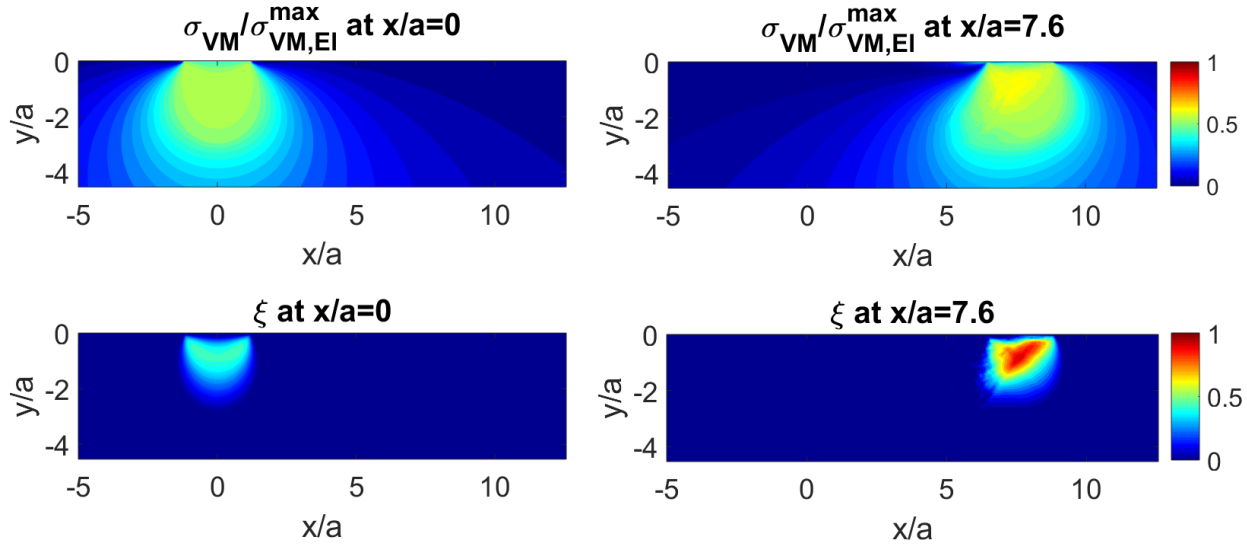


Figure 3.3: Normalized $\sigma_{VM}$ (top) and $\xi$ (bottom) in the half-space during different stages of sliding contact for $T > A_f$.

For the normal indentation step, the von Mises stress distribution is symmetric about $x/a = 0$, which is also position of the center of the cylinder. The presence of the large recoverable transformation strain causes the stress to be distributed over a larger region when compared to the stress distribution generated for the equivalent elastic contact problem. The maximum von Mises stress in the SMA half-space at this indentation depth is 0.57 times the maximum von Mises stress in the elastic half-space. This demonstrates the ability of the transformation strain in the SMA half-space to release some of the stress generated upon indentation.

This sliding response at $T > A_f$ is characterized by a complete recovery of austenite from the indentation induced martensite. This is demonstrated in Figure 3.3 in which the martensite volume fraction $\xi$ around the region of the initial indent ($x/a = 0$) is 0, indicating that the phase of the material reverted back to the austenitic phase upon unloading of the cylinder. During steady state frictionless sliding there is a noticeable increase in the von Mises stress and the martensite volume fraction. This response differs from frictionless steady state sliding of elastic materials where the stress distribution is almost the same as the stress distribution developed at indentation. It is also

synonymous with the gradual increase in the tangential force experienced by the indenter during sliding. At steady state sliding, the von Mises increases to about 0.65 times the maximum von Mises stress in the elastic half-space.

The SMA von Mises stress distribution and martensite volume fraction in a region of the half-space at $T$=275 K, which is just below $A_f$ but greater than $A_s$, is shown for the indentation and steady state sliding stages in Figure 3.4. At $\Delta x/a = 0$, the indentation step, the region of stress induced martensite is much larger than the region observed in Figure 3.3. This is explained by the fact that the stress required to induce martensite decreases as the operating temperature reduces (in accordance with the Clausius-Clapeyron relation). The maximum von Mises stress in the half-space at this analysis step is 0.47 times the maximum von Mises stress in the elastic half-space. This demonstrates that reducing the critical transformations stress for phase transformation leads to a lower effective stress in the half-space, which decreases the onset of plasticity.

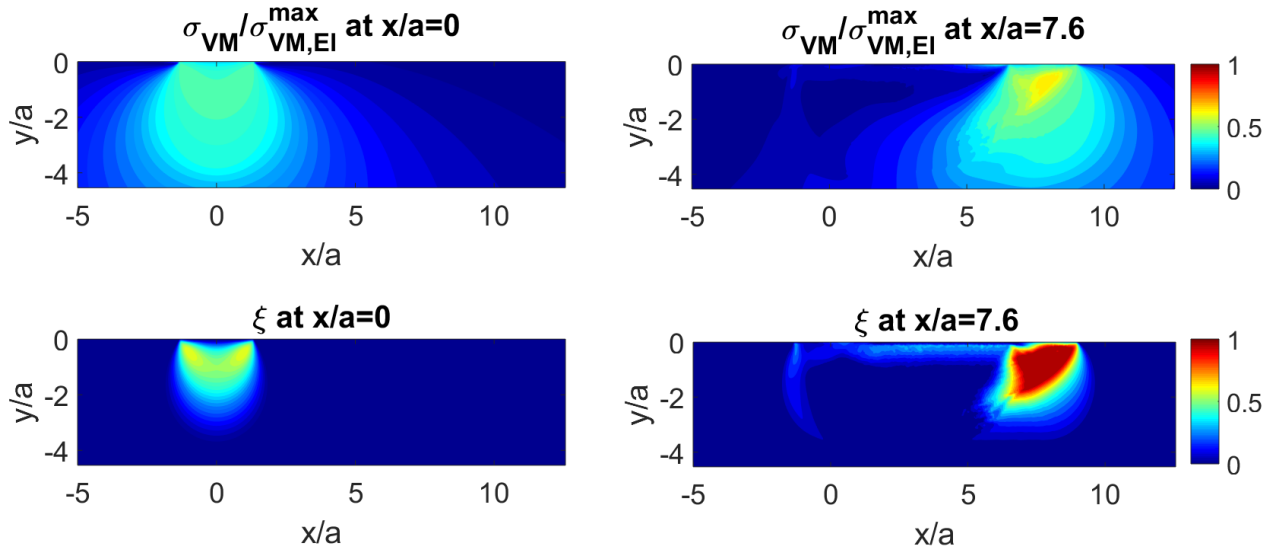


Figure 3.4: Normalized $\sigma_{VM}$ (top) and $\xi$ (bottom) in the half-space during different stages of sliding contact for $A_f < T < A_s$.

As in the previous case, there is an increase in $\xi$ and the maximum Mises stress at steady state

sliding $\Delta x/a = 7.6$. In this instance however, a complete reverse transformation to austenite does not take place when the cylinder unloads from the initial indentation and moves to the right as exhibited by the small amount of residual martensite in the region where the indentation occurred and in the wake of the sliding cylinder. At steady state sliding, the maximum Mises stress in the SMA half-space is approximately 0.67 times the maximum von Mises stress in the elastic half-space.

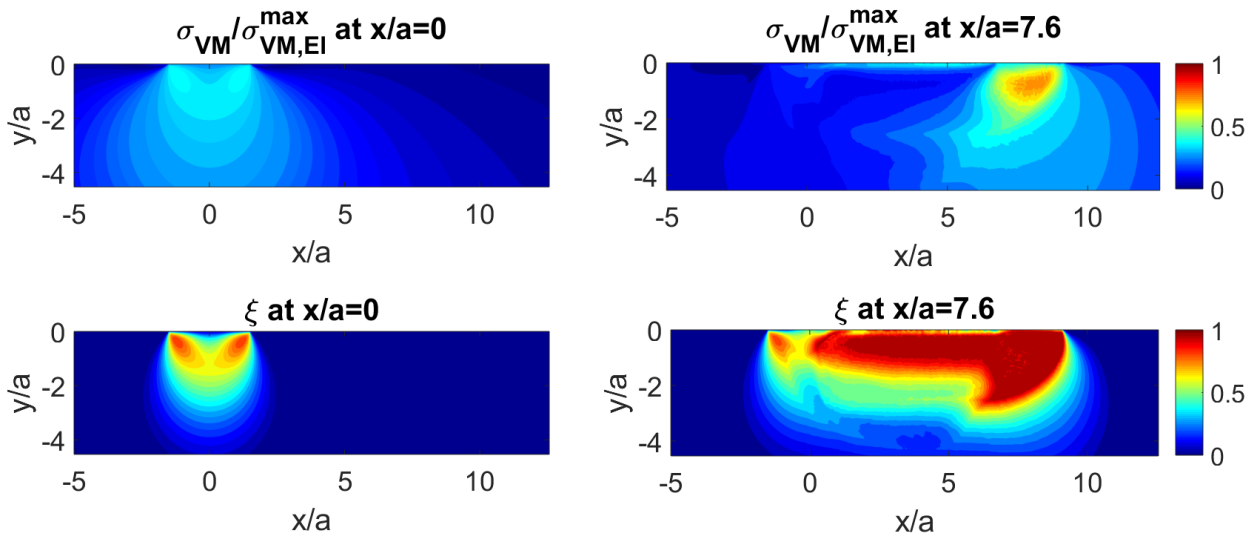


Figure 3.5: Normalized $\sigma_{VM}$ (top) and $\xi$ (bottom) in the half-space during different stages of sliding contact for $A_s < T$.

Figure 3.5 compares the normalized von Mises stress distribution and corresponding martensite volume fraction in the SMA half-space at different stages of the sliding process for an operating temperature $T$=265 K, which is just below $A_s$. A comparison of the indentation response ($x/a = 0$) for the three different isothermal loading paths shows that the region of stress induced martensite is largest in the latter case, while the von Mises stress is also the lowest in the latter case. This is expected as the indentation depth is kept constant for all three simulations and the reduction in the critical transformation stress as the temperature decreases, results in a higher degree of transformation at the lowest specified temperature.

Table 3.2: Normalized maximum von Mises stress $\sigma_{VM}/\sigma_{VM,El}^{max}$ at indentation and at steady state sliding for different isothermal loading paths ($H^{max} = 2\%, \mu = 0$).

| | $T > A_f$ | $A_s < T < A_f$ | $A_s < T$ |
|---|---|---|---|
| Indentation ($\Delta x/a = 0$) | 0.57 | 0.47 | 0.39 |
| Sliding ($\Delta x/a = 7.6$) | 0.65 | 0.67 | 0.78 |

During steady state sliding, it is observed that there does not appear to be any recovery to austenite upon unloading and a complete forward transformation to martensite is achieved. Furthermore, the region of residual stresses is significantly larger than in the temperature range of $A_s < T < A_f$. As a consequence of the build-up of the residual stresses at this temperature, the maximum von Mises stress in the SMA half-space increases from $0.39\sigma_{VM,El}^{max}$ during indentation to $0.78\sigma_{VM,El}^{max}$ at steady state sliding. These results for the different temperatures are summarized in Table 3.2.

The effect of the operating temperature during sliding contact is more apparent when analyzing the evolution of the surface displacement of the half-space between the indentation step and the steady sliding step. Figure 3.6 plots the normalized surface displacements for both analysis steps.

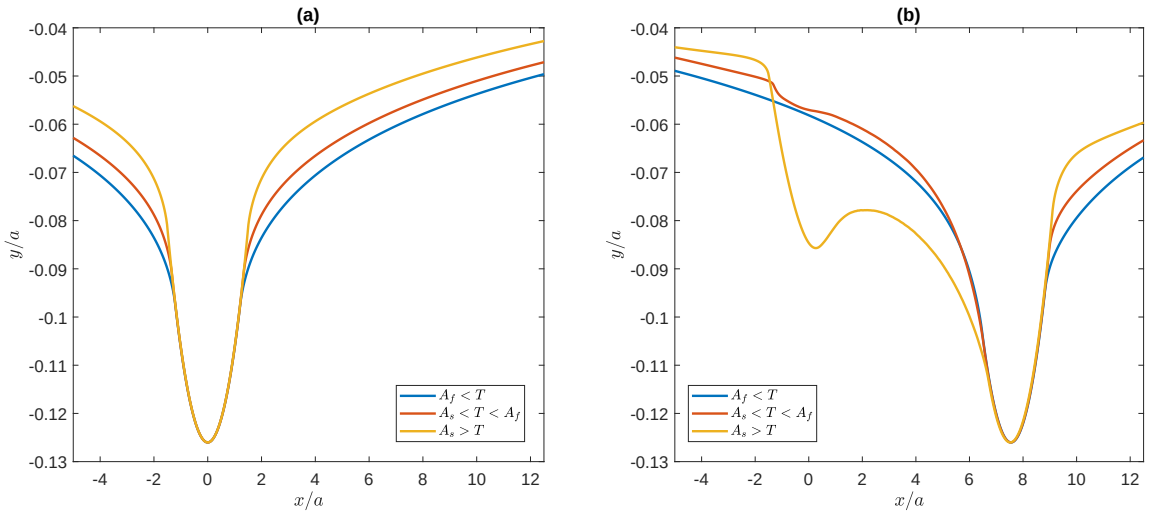


Figure 3.6: Comparison of surface displacements at different isothermal loading paths after (a) indentation and during (b) steady state sliding.

It is important to remember that the total surface displacement is a sum of the elastic displacement as well as the displacement due to phase transformation. In the indentation step, the maximum surface displacement of the half-space for all isothermal loading paths is the same due to the prescribed displacement boundary condition. After sliding to a distance away from the initial indent, there is a complete recovery of the initial indent generated due to both elastic and pseudoelastic deformation for $T > A_f$ while some small residual displacement persists for the case when $A_s < T < A_f$. A larger residual displacement at $x = 0$ is observed due to irrecoverable transformation strain when $A_s > T$. A portion of the recovery at this temperature is elastic. Experimentally, recovery of this residual displacement is possible by heating the sample above $A_f$ as shown for the case of pure indentation in the works of Ni et al. [58, 59]. This has also been demonstrated numerically by Nolan et al. [60] using the current constitutive model. This effect is not considered in this study as the primary focus is on the pseudoelastic behavior rather than the shape-memory behavior of these alloys.

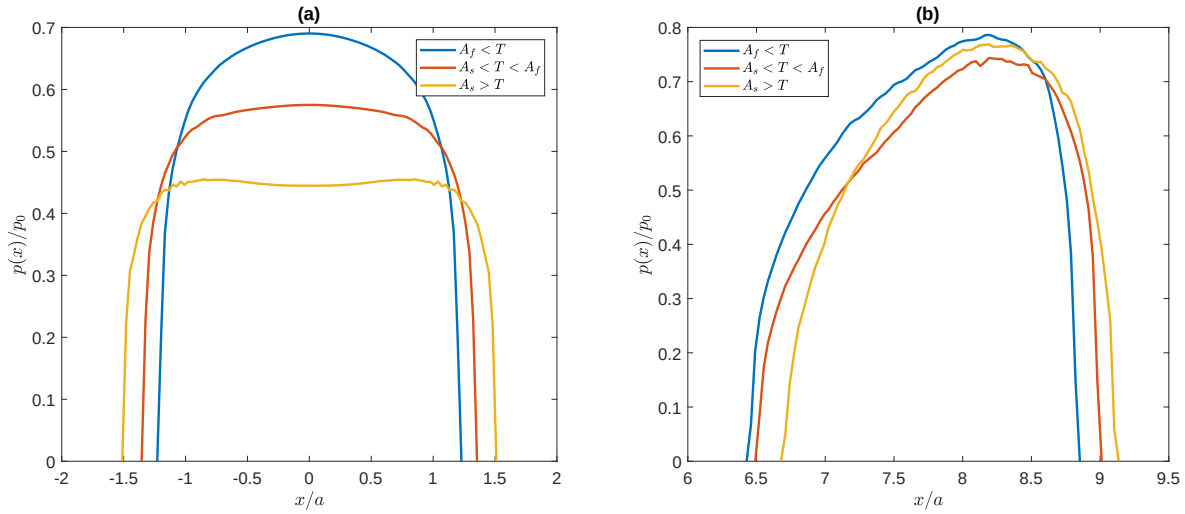


Figure 3.7: Comparison of the contact pressure distribution at different isothermal loading paths after (a) indentation and during (b) steady state sliding.

The surface contact pressure distribution due to indentation and during sliding at different

operating temperature regimes is shown in Figure 3.7. The contact pressure shown is normalized by the maximum Hertzian contact pressure $p_0$ caused due to indentation of an elastic material by the same displacement imposed boundary condition and with the same elastic properties as austenite. This normalization is chosen to illustrate the difference between a pseudoelastic and elastic contact pressure distribution. The contact pressure profile in indentation is symmetric about the $x = 0$ axis. In comparison to the contact pressure distribution obtained in a typical Hertzian elastic contact problem (see Figure 2.5), the maximum pseudoelastic contact pressure is much lower than the maximum elastic contact pressure distribution. It is also observed that a reduction in the temperature results in a reduction in the maximum contact pressure and a corresponding increase in the contact area. This reduction occurs due to fact that as the temperature decreases, the phase transformation occurs not only in the interior of the half-space but extends to the surface of the half-space that is contact with the cylinder. As the transformation zone around the region of contact increases, a larger contact area develops which leads to a reduction in the contact pressure. This is especially true for the case when $T < A_s$ and the SMA behaves similar to that of an elastic-plastic material. Simulations of the contact pressure distribution for elastic-plastic materials reveal a similar trend wherein a flattening of the contact pressure distribution occurs during indentation [18].

During frictionless steady state sliding, the contact pressure distribution is no longer symmetric about the indenter's center. This trend is markedly different from the contact pressure profile for elastic materials for which the contact profile remains symmetric and unchanged even during frictionless sliding (since tangential tractions are absent). For the pseudoelastic SMA, the maximum contact pressure increases in each case and shifts to the right of the indenter's center (in the direction of sliding). A significant jump in the contact pressure occurs for the case when $T < A_s$. In this specific case, the transformation zone has spread to the surface of the contacting region and in fact, a portion of the region in contact has completely transformed to martensite. Depending on the degree of transformation at the surface, the contact pressure distribution will not be uniform. This can be understood from an analytical point of view, since the Hertzian contact pressure distribution

(Equation 2.11) depends on several factors such as the elastic moduli of the bodies in contact, the radii of the contacting bodies and the applied load/displacement. Since in this instance, the elastic modulus of the half-space at the surface is not uniform, this results in an irregular contact pressure distribution.

### 3.2 Effect of Maximum Recoverable Transformation Strain

In this section, the influence of the maximum transformation strain on the sliding response is studied. The temperature $T$ is held constant above $A_f$ , while the coefficient of friction $\mu$ is assumed to be 0 (frictionless). $H^{max}$ is varied from 1% to 4% and effects of this variation on the von Mises stress and contact pressure are discussed. The constitutive responses of a single finite element for the different strains varied from 1%-4% are shown in Figure 3.8 to illustrate the implication this variation has on the stress-strain response.

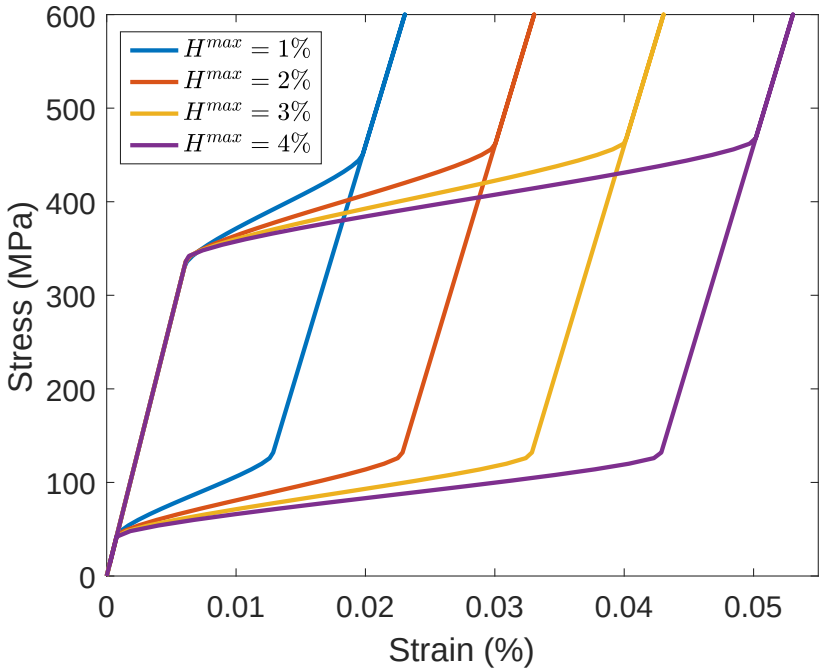


Figure 3.8: Constitutive response when $H^{max}$ is varied from 1% -4%.

The constitutive response obtained in Figure 3.8 is achieved by fixing the transformation temperatures and the slopes ($C^A$ and $C^M$) of the stress-temperature relationships in the phase diagram. The only parameter in the model that is varied is $H^{max}$. This renders the critical transformation stresses constant while the hardening decreases as $H^{max}$ increases.

In the finite element sliding simulation, the cylinder is initially at $x = 0$ and indents the half-space to a depth of $\Delta y = 0.008R$, which is deeper than the indentation depth specified in the previous simulation. This is followed by maintaining the same indentation depth and sliding to a distance of $\Delta x = 0.225R \approx 4.6a$, where $a$ is contact radius of a rigid cylinder indenting and sliding along an elastic half-space to same depth $\Delta y$ and with elastic properties equivalent to that of the austenitic phase. The sliding distance is once again chosen so as to attain a steady state stress distribution that is unaffected by the initial indentation. It is determined by studying the evolution of the tangential and normal reaction forces experienced by the cylinder during the sliding process.

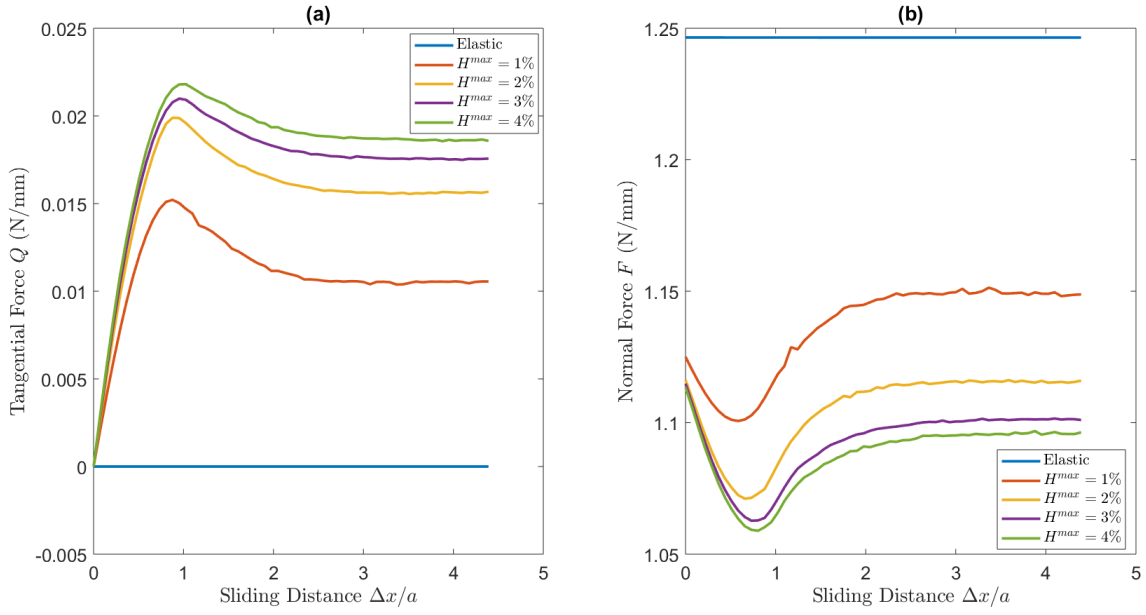


Figure 3.9: Reaction forces on the indenter at different half-space maximum transformation strains $H^{max}$ throughout the frictionless sliding process (a) tangential distributed force (b) normal distributed force.

Figure 3.9 shows the normal and tangential forces acting at the reference point of the rigid cylinder throughout the sliding process. In comparison with Figure 3.2, the magnitudes of the forces here are much higher as a consequence of the increase in the indentation depth. A similar trend is also observed in that there is a gradual increase in tangential force as the sliding step commences, before eventually decreasing and attaining a steady state value at about $\Delta x/a$=3. It is observed that an increase in the maximum transformation strain causes an increase in the distributed tangential force.

The difference between the pseudoelastic and elastic normal reaction force is much more pronounced at this indentation depth than seen in Figure 3.2. The smaller reaction force for contact between the indenter and the pseudoelastic half-space suggests that work done by the indenter during indentation and sliding is less than that for an elastic material. The decrease in the normal force during the initial stages of sliding corresponds with the increase in the tangential force at the same instance. The magnitude of the normal force decreases as the maximum transformation strain increases implying the ease of penetration of the indenter into the half-space as $H^{max}$ increases.

Since these simulations are conducted at $T > A_f$ , the evolution of the normalized von Mises stress and the martensite volume fraction follow a similar trend as observed in Figure 3.3, i.e., a complete reverse transformation to austenite is obtained as the cylinder unloads during the sliding process. Therefore, for the sake of brevity, only the results for region symmetric about the position of the indenter are shown for the post indentation and sliding steps.

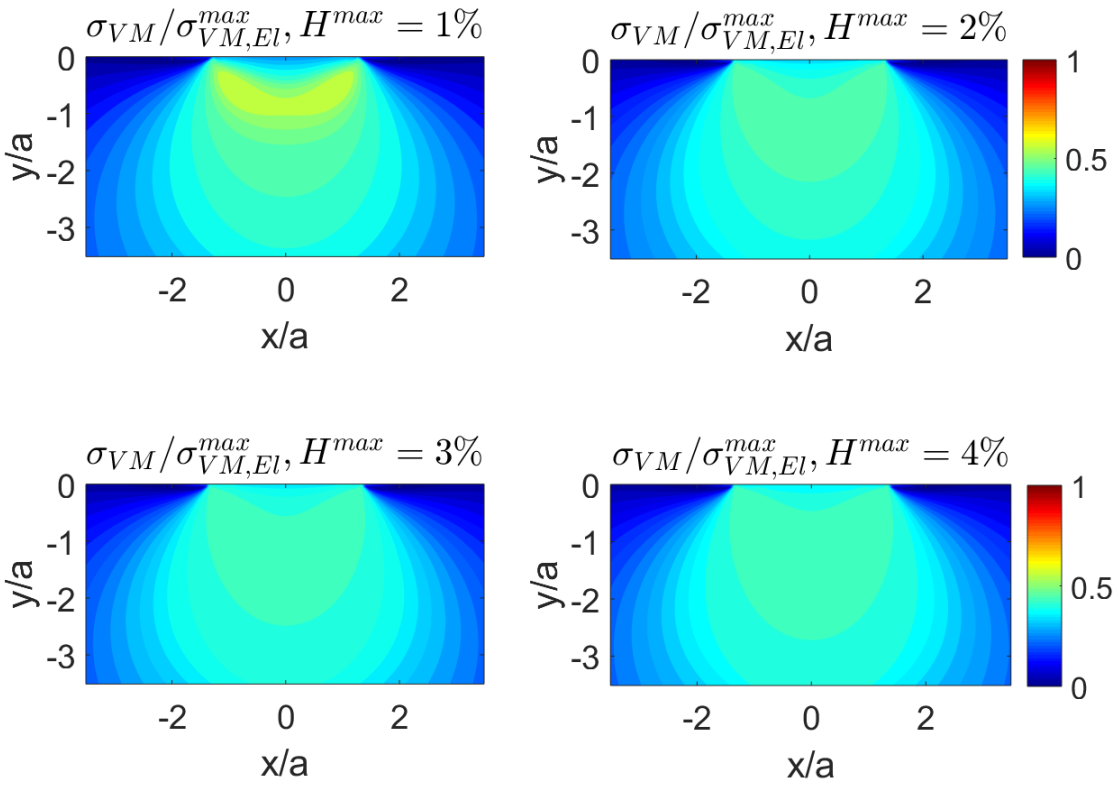


Figure 3.10: Normalized von Mises stress in the pseudoelastic half-space after indentation for various $H^{max}$ values (1%-4%) at an indentation depth of $\Delta y = 0.008R \approx 0.15a$.

A comparison of the von Mises stress developed after indentation for the different maximum transformation strains is shown in Figure 3.10. The results are normalized by the maximum von Mises stress $\sigma^{El}_{VM}$ developed by the indentation of a rigid cylinder into an elastic half-space with the same elastic properties as the austenitic phase. This is done so as to measure the difference between the response of a material without phase transformation and with phase transformation. The spatial dimensions of the pseudoelastic half-space are also normalized by the known analytical contact radius $a$ of the elastic half-space. In both the elastic case and the pseudoelastic case, the same indentation depth is specified ($\Delta y = 0.008R \approx 0.15a$).

Figure 3.10 shows that an introduction of even a small amount of transformation strain causes a large reduction in the maximum normalized Mises stress. For instance, the ratio of the maximum pseudoelastic von Mises stress with 1% recoverable strain to the maximum elastic von Mises stress

is 0.6. This represents a nearly 40% reduction in the maximum stress. This ratio is about 0.45 when $H^{max}$ is increased to 4% , which represents a 55% reduction in the stress. The ratio of the maximum pseudoelastic von Mises to its elastic analogue at 2% strain and 3% recoverable transformation strain are 0.473 and 0.458 respectively, which represent a decrease of about 50% in each case.

The martensite volume fraction in the half-space at the corresponding transformation strains is also shown in Figure 3.11 and offer some insight into the von Mises stress distribution in the half-space shown in Figure 3.10. For the same indentation depth, a complete transformation to martensite is achieved at $H^{mx} = 1\%$, while martensite is still in the detwinning process at higher maximum transformation strain values.

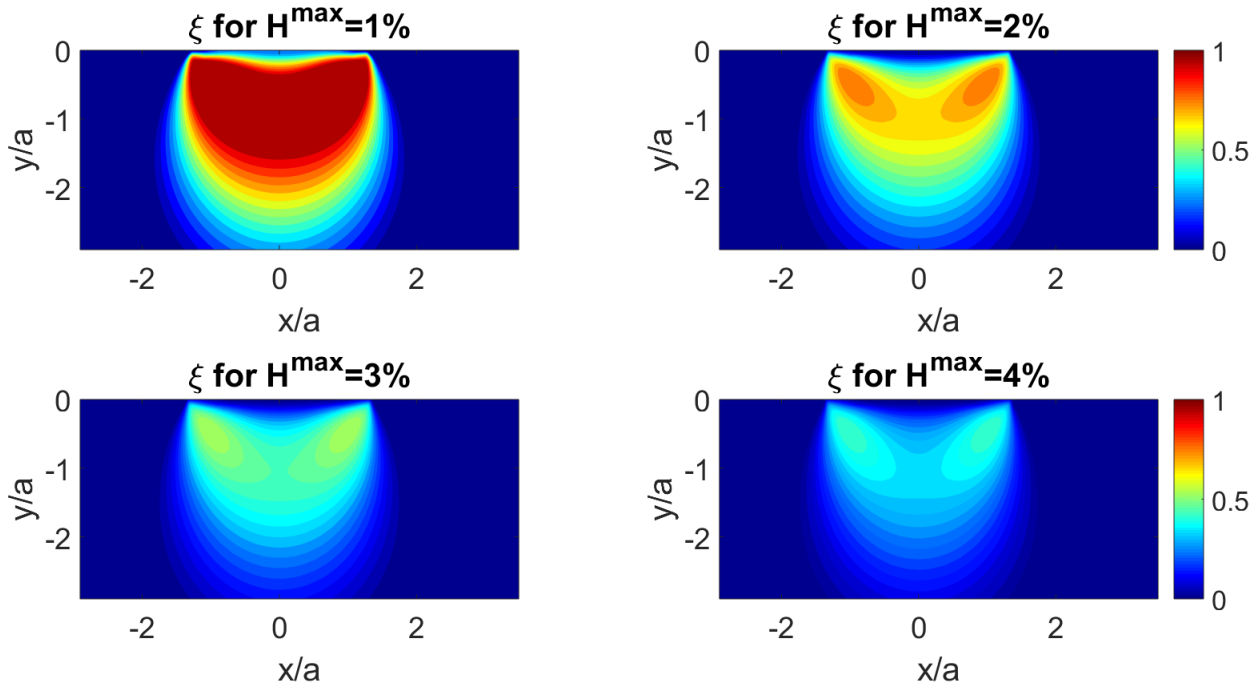


Figure 3.11: Martensite volume fraction in the pseudoelastic half-space after indentation for various $H^{max}$ values (1%-4%) at an indentation depth of $\Delta y = 0.008R \approx 0.15a$.

During the frictionless sliding phase, there is perceptible increase in the Mises stress (Figure

3.12). At steady state sliding, the ratio of the maximum pseudoelastic von Mises stress to the maximum elastic von Mises stress increases to about 0.85, representing only a 15% reduction in the stress. The largest reduction in the stress again occurs when $H^{max}$ is greatest, i.e., 4%. The ratio of the Mises stresses in this case is about 0.51, representing a 49% reduction in the stress in the half-space. For the case when $H^{max}$ is 2% and 3%, the ratios are 0.69 and 0.55. These results are summarized in Table 3.3. This can be further understood by studying the martensite volume fraction that correspond to these stress distributions.

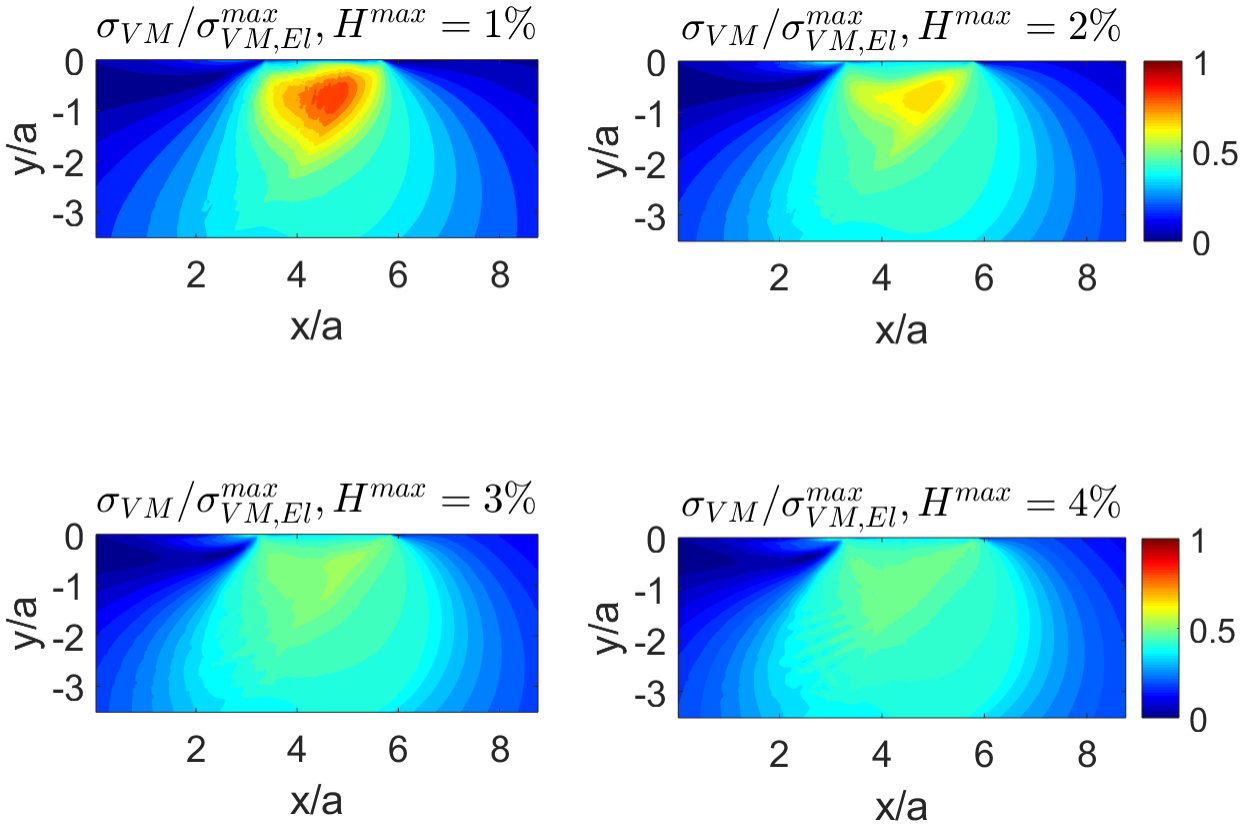


Figure 3.12: Normalized von Mises stress in the pseudoelastic half-space at steady state sliding for various $H^{max}$ values (1%-4%) at an indentation depth of $\Delta y = 0.008R \approx 0.15a$.

Figure 3.13 demonstrates that during steady state sliding, a complete transformation to martensite is achieved in all cases except for the case when $H^{max}$ is 4%. Furthermore, the region of

Table 3.3: Normalized maximum von Mises stress $\sigma_{VM}/\sigma_{VM,El}^{max}$ at indentation and at steady state sliding for different $H^{max}$ values ($T$=285 K,$\mu = 0$).

| | $H^{max} = 1\%$ | $H^{max} = 2\%$ | $H^{max} = 3\%$ | $H^{max} = 4\%$ |
|---|---|---|---|---|
| Indentation ($\Delta x/a = 0$) | 0.58 | 0.47 | 0.46 | 0.45 |
| Sliding ($\Delta x/a = 4.6$) | 0.85 | 0.69 | 0.55 | 0.51 |

martensite developed gets progressively smaller as $H^{max}$ increases. This suggests that SMAs with a high degree of pseudoelasticity can accommodate more of the imposed deformation by the cylinder and resist complete transformation to martensite and the eventual onset of plasticity.

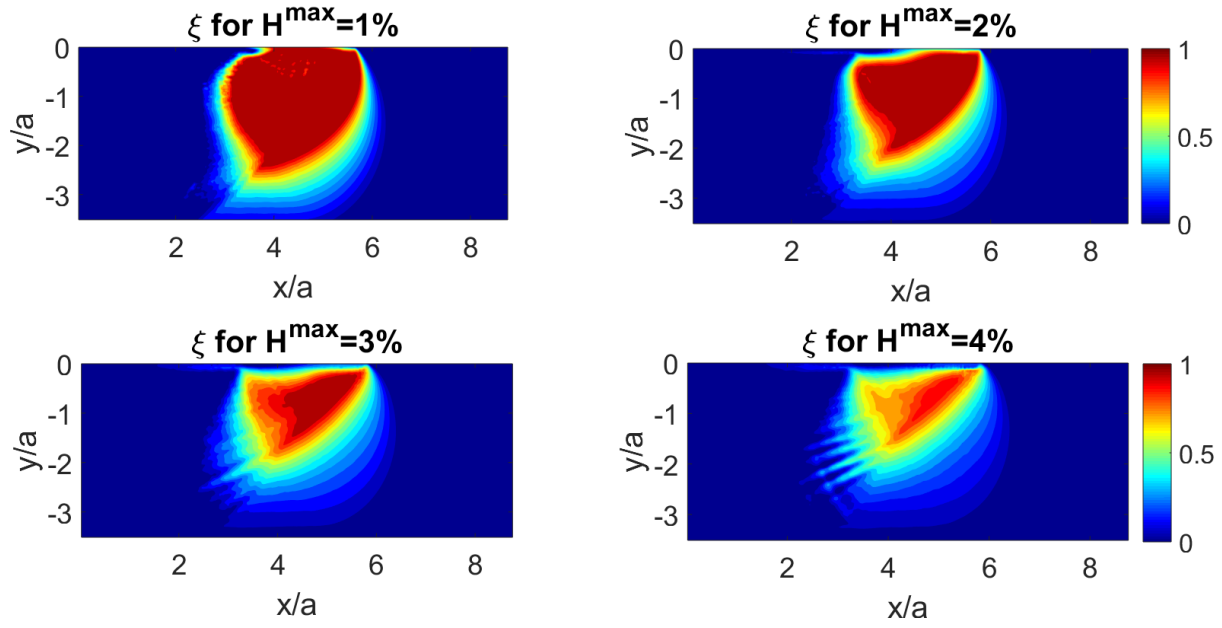


Figure 3.13: Martensite volume fraction in the pseudoelastic half-space at steady-state sliding for various $H^{max}$ values (1%-4%) at an indentation depth of $\Delta y = 0.008R \approx 0.15a$.

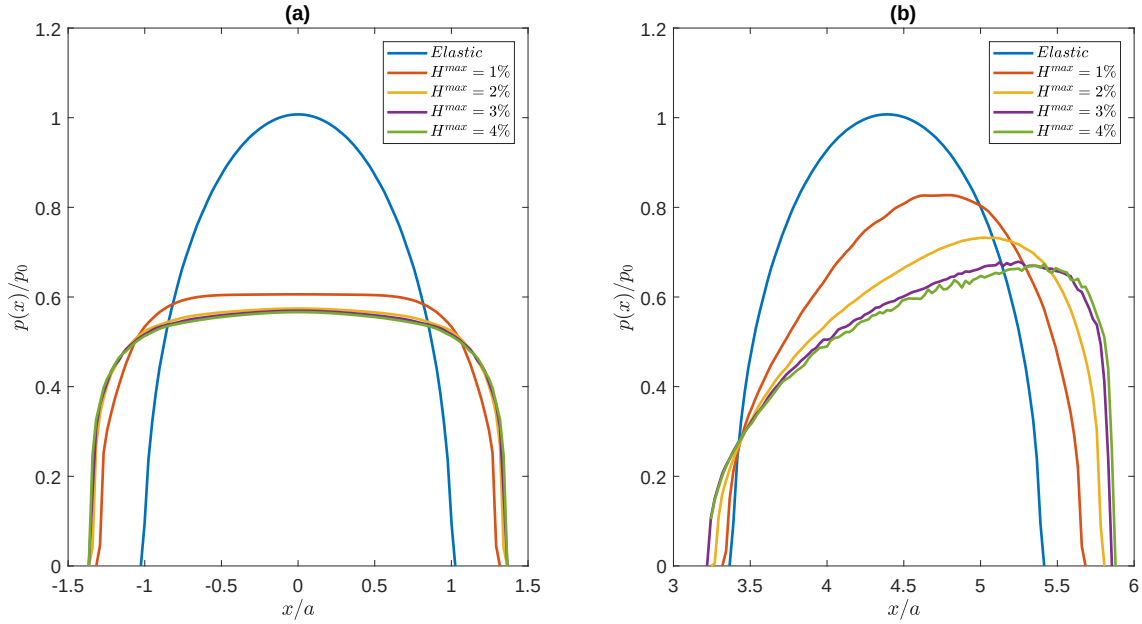


Figure 3.14: Comparison of the contact pressure distribution for various $H^{max}$ values (1%-4%) after (a) indentation and during (b) steady state sliding.

The contact pressure distribution for the variation in $H^{max}$ is shown in Figure 3.14 and is compared with the elastic Hertzian solution. All the contact pressure distributions are normalized by the maximum contact pressure $p_0$ at the surface of an austenitic half-space ($E = 55$ GPa, $\nu = 0.3$). It becomes quite apparent that the presence of pseudoelasticity in the half-space results in a non-Hertzian contact pressure distribution. An increase in $H^{max}$ corresponds to an increase in the contact area, which results in a decrease in the contact pressure. However, the decrease in the maximum contact pressure does not follow a linear trend, indicating that at some maximum $H^{max}$ value, the contact area and pressure distribution will remain unchanged. This is especially observed when comparing the contact pressure distributions when $H^{max} = 3\%$ and 4%. Figure 3.11 shows that at these transformation strains, the distribution in the internal state variable $\xi$ is different. The greater the value of $\xi$ is in the contact region, the greater is the maximum contact pressure distribution.

During frictionless sliding contact, the contact pressure distribution is asymmetric and in-

creases in the direction of the sliding. When compared to the contact pressure distribution at $\Delta x/a = 0$, the maximum contact pressure during steady state sliding is much higher, while the elastic contact pressure distribution is still Hertzian (symmetric). This trend is characterized by the absence of any tangential force $Q$ on the indenter during elastic sliding contact and a non-zero $Q$ on the indenter during pseudoelastic sliding contact (see Figure 3.9). This increase in the contact pressure in the half-space and tangential force on the indenter from pseudoelastic normal contact to pseudoelastic sliding contact is a consequence of the steady increase in the martensite volume fraction $\xi$ at the contact surface (Figure 3.13), which changes for different the loading conditions and various $H^{max}$ values.

### 3.3 Effect of Modulus Change

The presence of two different elastic moduli in the half-space can lead to a very different stress field in the half-space when compared to a homogeneous elastic half-space. This is well established especially when considering contact mechanics literature of layered elastic half-spaces with different properties [20, 21, 61, 62]. Typical elastic properties of the austenite and martensite phases in pseudoelastic materials can differ greatly, with the modulus of martensite being lower than that of austenite. This difference is quantified by the parameter $\beta$ which represents the ratio of the elastic modulus of the martensite phase to the austenitic phase. Kan et al [63] have shown that this ratio is typically in the range of $0.3 - 0.65$ for most SMAs. In this study, the ratio of $\beta$ is varied from 0.5 to 1 and its effect on the stress distribution in the half-space is studied.

The constitutive responses of a single finite element for the various $\beta$ values are shown in Figure 3.15 to illustrate the implication this variation has on the stress-strain response.

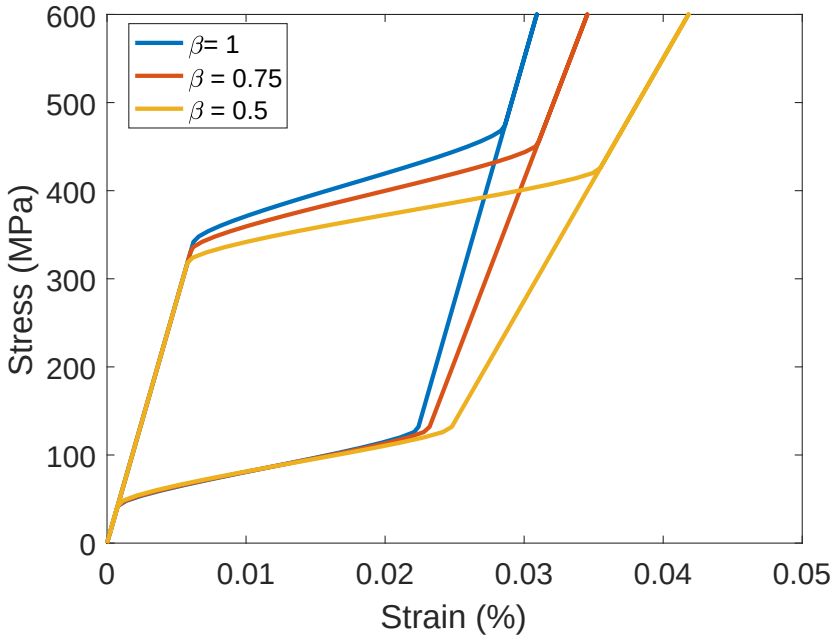


Figure 3.15: Constitutive response for different $\beta = \frac{E_M}{E_A}$.

The effect of this difference in the elastic moduli is studied under both normal and steady state sliding contact. In all simulations, the parameter $H^{max}$ is fixed at 2% and the temperature is held constant at $T > A_f$. The decrease in $\beta$ is accompanied by a softening response and a pronounced decrease in the martensite finish stress $\sigma_{Mf}$.

The Mises stress for the different $\beta$ values considered is shown in Figure 3.16. The stress is once again normalized by the maximum Mises stress developed in an elastic half-space in normal contact with a rigid cylinder to the same indentation depth as the pseudoelastic half-space. This normalization is chosen in an attempt to compare the difference between the contact behavior of pseudoelastic and elastic materials.

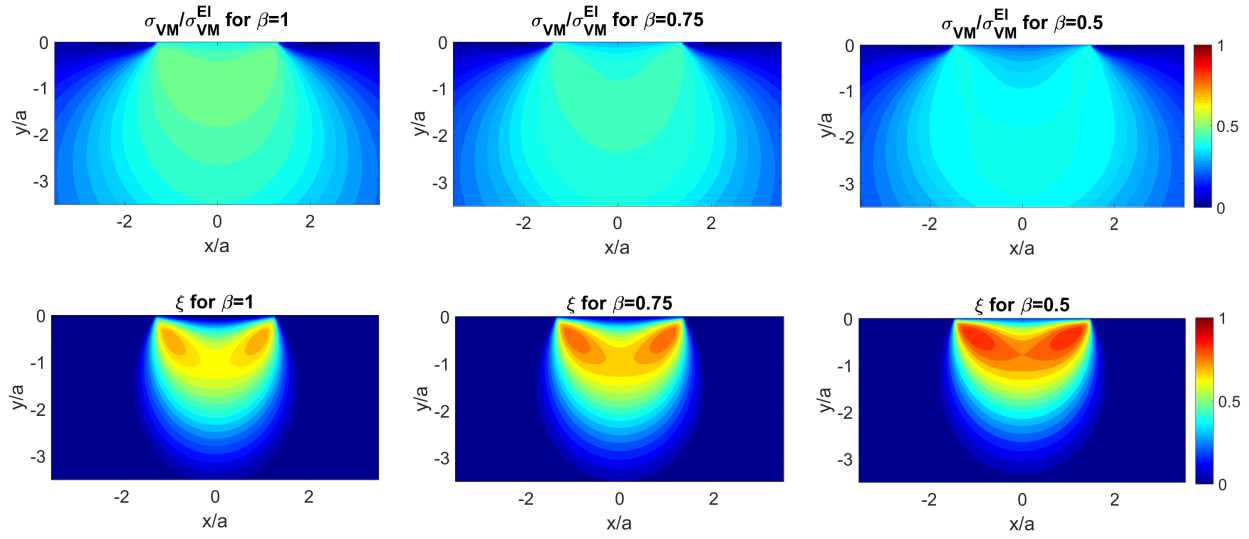


Figure 3.16: Normalized von Mises stress and martensite volume fraction in the pseudoelastic half-space after indentation for various $\beta$ values.($\Delta y = 0.008R \approx 0.15a$, $H^{max} = 2\%$, $T = 285K$).

It is observed that as the $\beta$ parameter increases, the von Mises stress in the half-space decreases. In fact, the maximum stress directly beneath the indenter significantly decreases as $\beta$ decreases. Naturally this is because as $\beta$ decreases, the half-space becomes more compliant. In quantitative terms, ratio of the maximum pseudoelastic von Mises stress to the elastic von Mises stress is 0.51 when $\beta = 1$. For this case, the elastic moduli of both austenite and martensite are the same as the modulus of the elastic material used for the normalization. The ratio of the Mises stresses falls to 0.46 and 0.41 for $\beta = 0.75$ and $\beta = 0.5$ respectively. These results are summarized in Table 3.4.

Figure 3.16 also illustrates the corresponding martensite volume fraction in the half-space, which demonstrates that as $\beta$ decreases, the martensite volume fraction $\xi$ increases. This is likely due to the fact that the constitutive behavior (Figure 3.15) predicts a reduction in the martensite finish stress $\sigma_{M_f}$ as $\beta$ increases. In other words, for the same fixed indentation depth, the indentation induced stress needed to completely transform to martensite is higher when $\beta$ is 1 as opposed to when $\beta$ is smaller.

Under steady state sliding, complete transformation to martensite is achieved in all cases. At

Table 3.4: Normalized maximum von Mises stress $\sigma_{VM}/\sigma^{max}_{VM,El}$ at indentation and at steady state sliding for different $\beta$ values ($T$=285 K,$\mu = 0$,$H^{max} = 2\%$).

| | $\beta = 1$ | $\beta = 0.75$ | $\beta = 0.5$ |
|---|---|---|---|
| Indentation ($\Delta x/a = 0$) | 0.51 | 0.46 | 0.41 |
| Sliding ($\Delta x/a = 4.6$) | 0.73 | 0.67 | 0.61 |

this analysis step, the maximum von Mises stress in all cases is nearly 40% higher than the corresponding maximum stresses after indentation. In keeping with the trend observed during indentation, the stress in the half-space during steady state sliding is smallest when the when the martensite phase is more compliant ($\beta = 0.5$). This ability of SMAs to undergo a transformation to a more compliant phase, further demonstrates why pseudoelastic SMAs offer better wear resistance that conventional wear resistant materials.

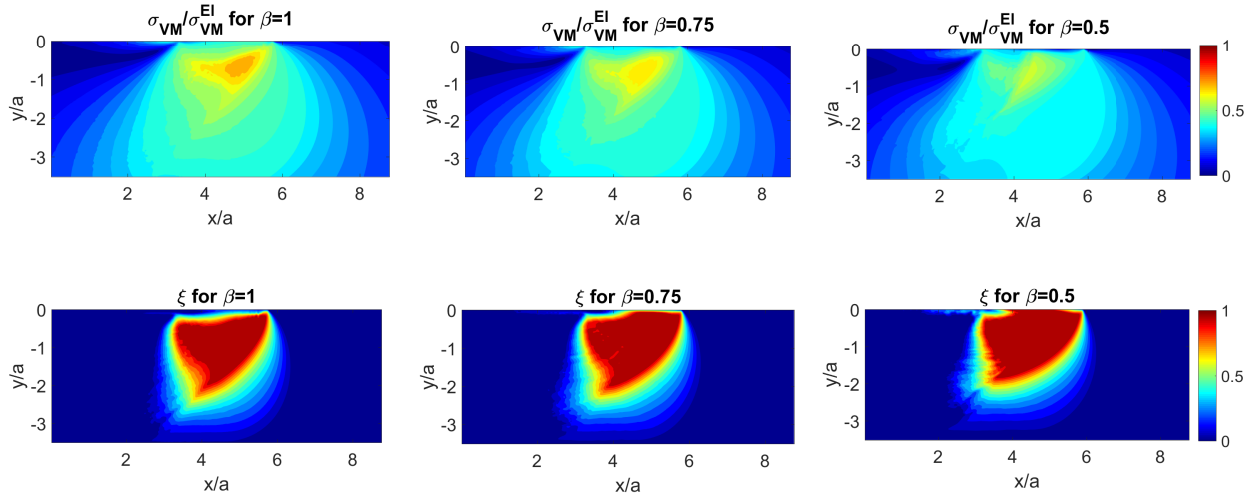


Figure 3.17: Normalized von Mises stress and martensite volume fraction in the pseudoelastic half-space during steady state sliding for various $\beta$ values. ($\Delta y = 0.008R \approx 0.15a$, $H^{max} = 2\%$, $T = 285K$).

The contact pressure distribution in the half-space at these different $\beta$ ratios is studied next (Figure 3.18). The contact pressure distribution in each case is normalized by the maximum con-

tact pressure $p_0$ developed at the contact surface between a rigid cylindrical indenter in normal contact with an elastic half-space ($E = 55$ GPa, $\nu = 0.3$) to an indentation depth of $\Delta y = 0.008R$. As the martensite phase becomes more compliant, the maximum contact pressure reduces and the contact area increases. This is observed for both the normal contact and steady state sliding contact pressure distributions. From a classical Hertzian contact mechanics approach, the maximum contact pressure $p_0$ is proportional to the elastic modulus of the half space (Equation 2.11). Therefore, the more compliant the half-space, the lower is the contact pressure.

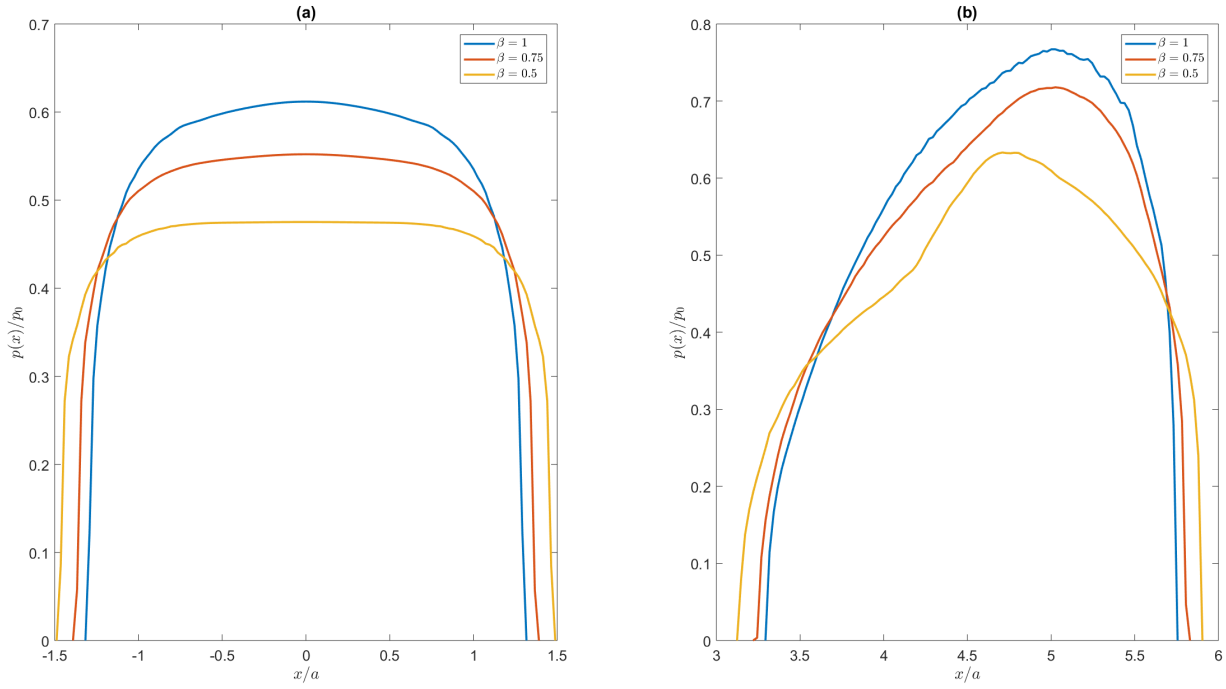


Figure 3.18: Comparison of the contact pressure distribution for various elastic mismatch ratios after (a) indentation and during (b) steady state sliding.

### 3.4 Effect of Friction

The previous simulation studies focused on the effect of pseudoelastic SMA relevant parameters on the frictionless sliding contact response. In this study, the effect of friction at the contact interface is studied for one of the SMA relevant parameters. Specifically, the effect of friction on

the sliding response at different isothermal loading paths is studied.

In the FEM simulations, two different coefficient of frictions $\mu = 0.15$ and $\mu = 0.25$ are employed to compare the effect of frictional pseudoelastic sliding contact against frictional elastic sliding contact ($\mu = 0$). In the first step, a normal displacement equal to $\Delta y/R = 0.004$ is specified at the reference point of the indenter and in the subsequent step, this normal displacement is held constant and a tangential displacement is specified equivalent to $\Delta x/R = 0.0275$. The same indentation depth and sliding distance are then specified for the frictional pseudoelastic simulations. The maximum transformation strain for the pseudoelastic half-space is chosen as $1\%$ and the Young's modulus for austenite and martensite are the same as those specified in Table 3.1.

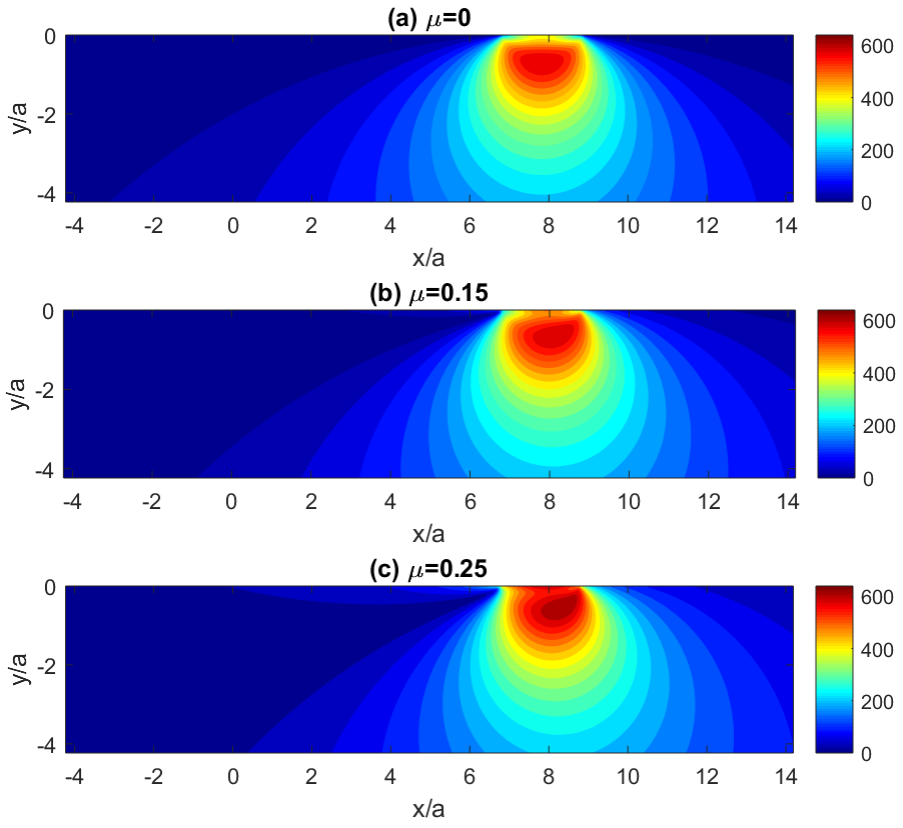


Figure 3.19: Comparison of the von Mises stress distribution in an elastic half-space for various friction coefficients $\mu$ at steady state sliding ($\Delta x/R = 0.00275$).

The elastic von Mises stress distribution during steady state sliding for the different coefficients of friction are shown first to demonstrate the effect of friction in an elastic sliding contact process (Figure 3.19). Two key observations are made, the first being that frictional sliding causes an asymmetric stress distribution in the elastic half-space. The second observation is that the maximum stress in the half-space increases as the coefficient of friction increases. For the frictionless sliding case, the maximum von Mises stress in the half-space is 588 MPa and increases to 596 MPa and 636 MPa for $\mu = 0.15$ and $\mu = 0.25$ respectively.

Having demonstrated the typical characteristics of frictional sliding contact for an elastic material, the frictional sliding contact of a pseudoelastic half-space at various temperatures are now presented. The same isothermal loading paths chosen in Section 3.1 are used here. The von Mises stress distribution in the pseudoelastic half-space for each frictional sliding contact simulation is normalized by the corresponding maximum von Mises $\sigma_{VM}^{El}$ stress in an elastic half-space and is shown in Figure 3.20.

As pointed out in the previous simulations, the frictionless sliding step produces an asymmetric stress distribution in the pseudoelastic half-space which is not the case for the frictionless sliding of the elastic half-space as shown in Figure 3.19 (a). This asymmetry in the stress distribution during sliding is compounded by the addition of the shear traction at the contact interface due to friction. The increase in the coefficient of friction causes an increases in the maximum von Mises stress in the half-space. In quantitative terms, the normalized Mises stress increases from 0.74 for $\mu = 0$ to 0.76 and 0.86 for $\mu = 0.15$ and $\mu = 0.25$ respectively. This indicates that as the friction at the contact interface increases, the ability of the pseudoelastic SMA to relieve the stress in the half-space diminishes.

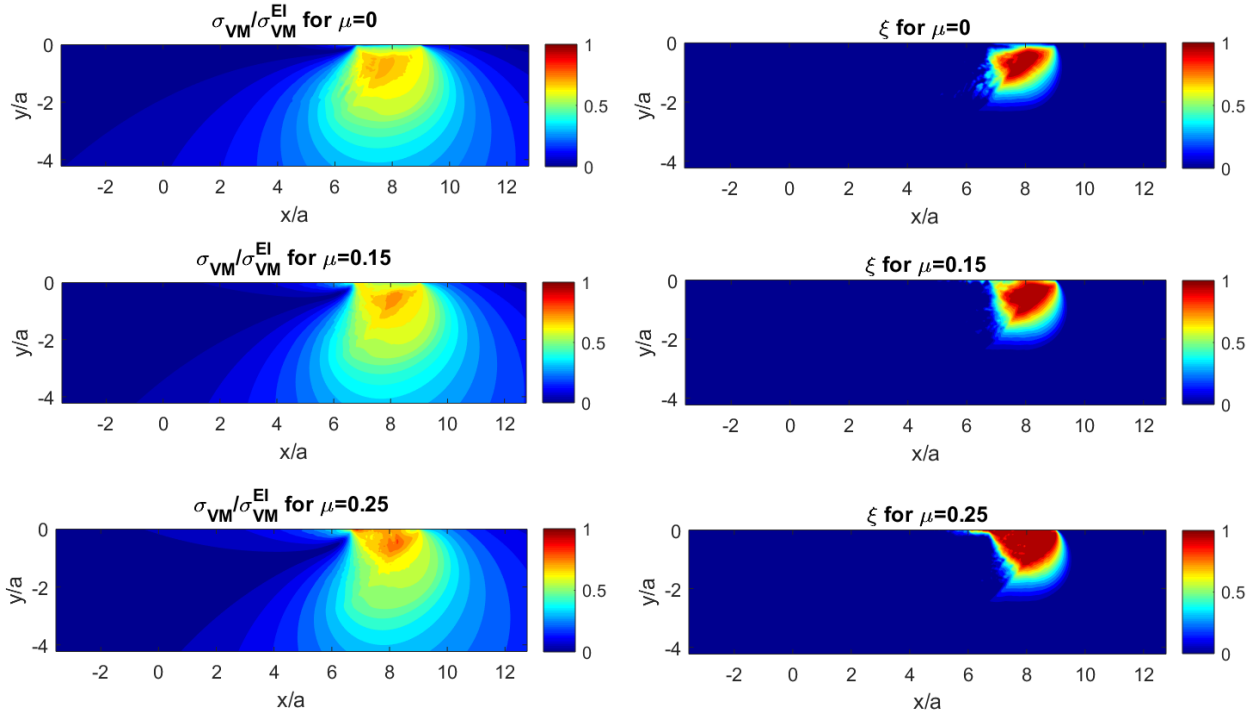


Figure 3.20: Normalized von Mises stress (left) and martensite volume fraction (right) in the pseudoelastic half-space for various friction coefficients $\mu$ at steady state sliding ($\Delta x/R = 0.00275, T = 285\text{K} > A_f$).

At low coefficients of friction, the maximum Mises stress develops in the interior of the half-space. This indicates that failure would likely originate in the interior of the half-space. For a higher coefficient of friction, $\mu = 0.25$, the maximum Mises stress moves from the interior of the half-space to the surface of the half-space and at the trailing edge of the sliding cylinder. A similar trend is also observed for the martensite volume fraction, where $\xi = 1$ in the interior of the half-space for low coefficients of frictions, but at $\mu = 0.25$, $\xi = 1$ both in the interior and the contact region. Johnson [4] states that for elastic materials, the von Mises criterion predicts that the transition from sub-surface yielding to surface yielding occurs when the coefficient of friction $\mu > 0.3$. Therefore for elastic materials, the maximum von Mises stress in the half-space moves from the interior to the surface at $\mu = 0.3$ during sliding. However, these simulations show that in the pseudoelastic case, the maximum von Mises stress moves from the interior to the surface at a slightly lower value $\mu = 0.25$. This likely due to the combination of the build-up of tensile stresses

at the trailing edge of the sliding cylinder due to friction and the inherent increase in the tensile stresses at the trailing edge observed even during frictionless pseudoelastic sliding.

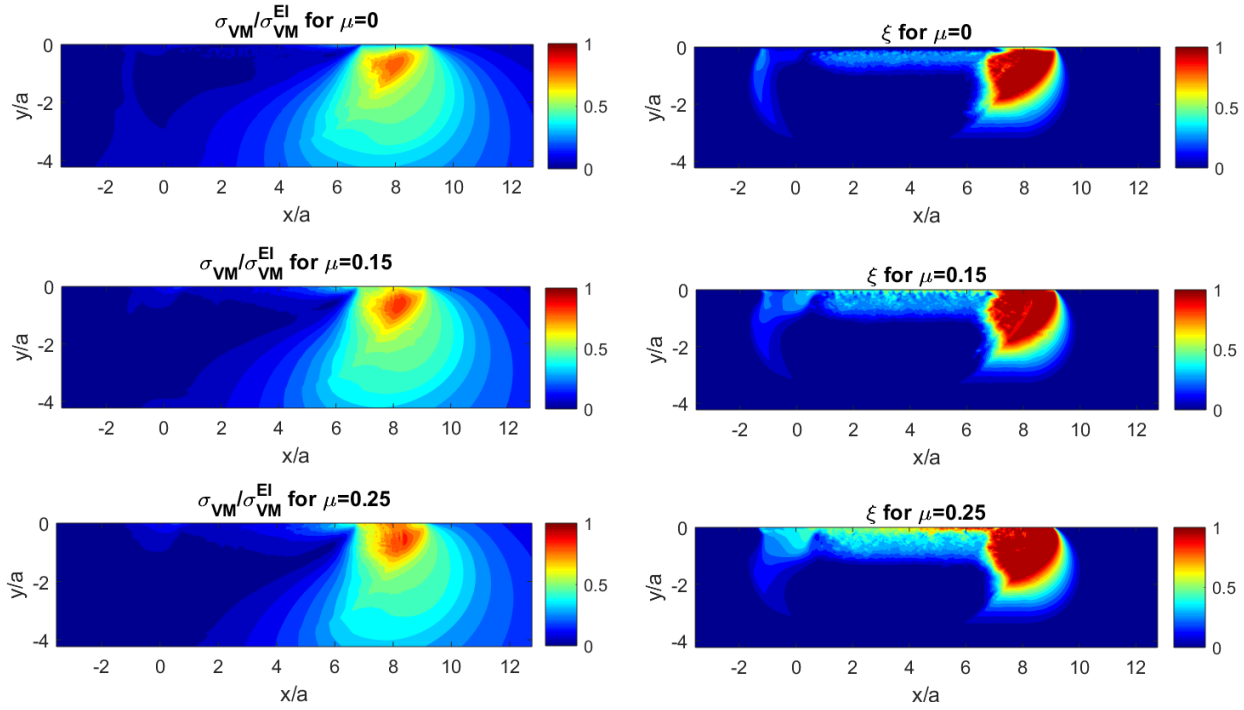


Figure 3.21: Normalized von Mises stress (left) and martensite volume fraction (right) in the pseudoelastic half-space for various friction coefficients $\mu$ at steady state sliding ($\Delta x/R = 0.00275, T = 275$ K $< A_f$).

Figures 3.21 and 3.22 show the frictional steady state sliding responses for isothermal loading at $A_s < T < Af$ and $T < A_s$. Once again, an increase in the coefficient of friction results in an increase in the maximum von Mises stress. The maximum normalized stresses are reported in Table 3.5. It is observed that as the coefficient of friction increases, the residual stresses that develop in the half-space as the cylinder unloads from the initial indentation location, are now more localized towards the surface of the half-space. For $\mu = 0$ for instance, residual stresses are present at depths of $y/a = -4$, but for $\mu = 0.25$, these residual stresses are absent. Frictional sliding contact of the elastic half-space has shown that as the coefficient of friction increases, the stresses in the vicinity of the contact region increase. This has an effect of increasing the volume

fraction of the residual martensite near the surface of the half-space as also shown in Figures 3.21 and 3.22.

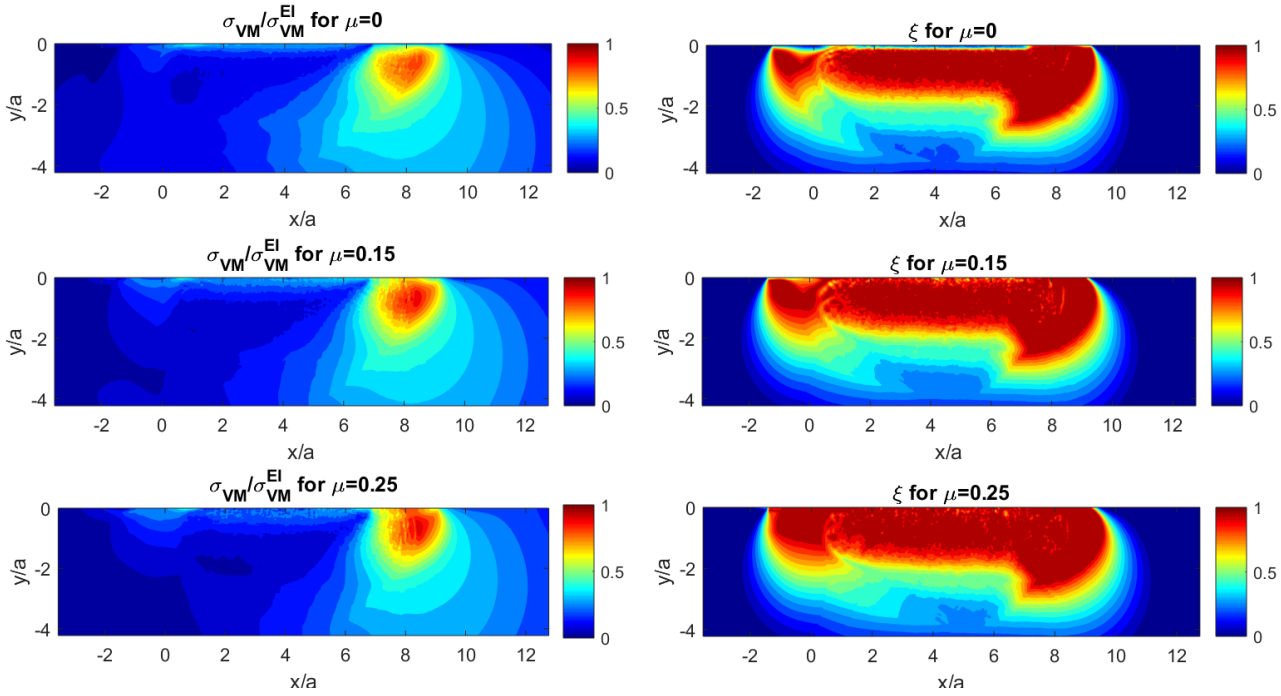


Figure 3.22: Normalized von Mises stress (left) and martensite volume fraction (right) in the pseudoelastic half-space for various friction coefficients $\mu$ at steady state sliding ($\Delta x/R = 0.00275, T = 265$ K $< A_s$).

Table 3.5: Normalized maximum von Mises stress $\sigma_{VM}/\sigma_{VM,El}^{max}$ at steady state sliding for different $\mu$ values ($H^{max} = 1\%$, $\beta = 0.84$).

| | $T > A_f$ | $A_s < T < A_f$ | $A_s < T$ |
|---|---|---|---|
| $\mu = 0$ | 0.74 | 0.81 | 0.86 |
| $\mu = 0.15$ | 0.76 | 0.87 | 0.93 |
| $\mu = 0.25$ | 0.86 | 0.89 | 0.95 |

# 4. CONCLUSIONS AND FURTHER STUDIES

This computational study involved the solution of the two dimensional plane strain sliding contact problem between a rigid cylindrical indenter and a pseudoelastic SMA half-space by using the finite element method. The SMA constitutive model put forward by Lagoudas et al. [53] is employed in conjunction with in-built contact algorithms in the commercial finite element software ABAQUS to simulate the combined normal and tangential contact between the two bodies. Normal and sliding contact are prescribed using a displacement controlled approach. Parametric studies involving the effect of unique SMA material characteristics (thermo-mechanical coupling, large recoverable strains, the inherent difference between the moduli of the martensite and austenite phases) on the pseudoelastic sliding contact behavior are investigated. In a separate study, the effect of friction between the two bodies is studied and its implications on surface wear for pseudoelastic materials are discussed.

## 4.1 Conclusion

The main conclusions from the parametric studies are listed here

- Indentation of the cylinder into the half-space causes phase transformation from austenite to martensite to initiate at a point directly below the center of the indenter and in the interior of the half-space rather than on the surface. This result is consistent with the elastic contact mechanics predictions that also show that the maximum von Mises stress in the half-space for normal contact with parabolic shaped indenters such as cylinders and spheres occurs at point in the interior of the half-space. As the normal displacement increases, the transformation zone spreads radially outwards until it reaches the surface of the half-space.

- During pseudoelastic sliding contact, the region in front of the indenter undergoes stress induced forward transformation to martensite, while the region in the wake of the indenter undergoes reverse transformation to austenite. The initial stages of frictionless sliding contact are associated with an increase in the von Mises stress distribution, which drives

an increase in the martensite volume fraction during sliding until a steady state sliding response is achieved. This suggests that even though complete transformation to martensite may not occur after indentation, the increase in stress during sliding could induce a complete forward transformation to martensite. This depends on several factors such as the depth of indentation, the amount of recoverable transformation strain and the elastic moduli the two phases.

- Half-spaces that are elastic undergo a symmetric translation of the stress developed at indentation during frictionless sliding contact. This is because the absence of friction does not permit any tangential traction in the contact region and the reaction forces due to the materials elasticity are very small. The FEM simulations show that for pseudo-elastic half-spaces, even during frictionless sliding contact at temperatures above $A_f$, a non-zero tangential component exists, which contributes to an asymmetric stress distribution in the half-space.

- The sliding contact behavior is heavily temperature dependent. According to the Clausius-Clapeyron relation, the decrease in temperature causes a decrease in the corresponding critical transformation stresses. As a result, for the same normal indentation depth, half-spaces at lower temperatures see a greater degree of transformation. At temperatures below $A_f$, a perfect pseudoelastic behavior is not observed, with residual displacement and residual stresses present in the half-space. At temperatures below $A_s$, the SMA behaves like an elastic-plastic material, with a flattened contact pressure distribution and significant residual stresses present in the wake of the sliding cylinder.

- Increasing the maximum transformation strain in the half-space results in a lower von Mises stress distribution during both normal and sliding contact. When compared to an elastic half-space with the same elastic properties as austenite, the presence of transformation strains as high as 4% can cause the maximum pseudoelastic Mises stress to differ from the maximum elastic Mises stress by about 55% when in normal contact. During frictionless sliding contact, this disparity is somewhat diminished as the stresses increase during sliding.

- The ability of shape memory alloys to transform from a high stiffness austenitic phase to a low stiffness martensite phase also contributes to the decrease in the von Mises stress. This stiffness difference is quantified by the parameter $\beta$ in this study and it is shown that as the difference between the two phases increases, the maximum Mises stress in the half-space and maximum contact pressure at the contact interface decreases.

- Therefore, the combination of high transformation strains and a low martensitic elastic modulus are significant parameters that reduce the von Mises stress in the half-space. This has important implications for the wear resistance of SMAs since worn surfaces contain very high levels of plastic strain compared to unworn surfaces. The accumulation of this strain and the consequent modification of the material's microstructure have a strong effect on the wear processes.

## 4.2 Further Study

A key outcome of this thesis was in demonstrating that a pseudoelastic SMA half-space in normal and tangential contact is capable of developing much lower stresses than an elastic half-space under similar applied displacements/tractions. It was demonstrated that this is a result of a combination of the operating temperature, presence of large recoverable transformation strains and phase transformation to a more compliant phase. The computational study adds valuable insight into the sliding behavior of phase transforming materials and agrees with experimental results that demonstrate the superior wear resistance of pseudoelastic SMAs under a typical sliding wear process. The literature review on the computational contact mechanics studies showed that the wear resistance of conventional materials can be improved by adding a hard coating or layer. Some researchers have also investigated the use of functionally graded coatings [64–66], where a power function is used to specify a spatial gradient in the material properties of the coating and substrate. In a similar fashion, the current work can be extended to include a spatial gradient in key SMA material parameters such as the transformation temperatures and transformation strains and thereby further reduce the maximum von Mises stress in the half-space.

# REFERENCES


[1] D. C. Lagoudas, *Shape memory alloys: modeling and engineering applications*. Springer Science & Business Media, 2008.

[2] H. Hertz, "On the contact of elastic solids," *Z. Reine Angew. Mathematik*, vol. 92, pp. 156–171, 1881.

[3] M. T. Huber, "Zur theorie der berührung fester elastischer körper," *Annalen der Physik*, vol. 319, no. 6, pp. 153–163, 1904.

[4] K. L. Johnson, *Contact mechanics*. Cambridge university press, 1987.

[5] J. Boussinesq, *Application des potentiels à l'étude de l'équilibre et du mouvement des solides élastiques: principalement au calcul des déformations et des pressions que produisent, dans ces solides, des efforts quelconques exercés sur une petite partie de leur surface ou de leur intérieur: mémoire suivi de notes étendues sur divers points de physique, mathematique et d'analyse*, vol. 4. Gauthier-Villars, 1885.

[6] S. P. Timoshenko and J. N. Goodier, *Theory of elasticity*, vol. 3. McGraw-Hill, New York London, 1970.

[7] A. C. Fischer-Cripps, *Introduction to contact mechanics*, vol. 101. Springer, 2007.

[8] E. Mcewen, "Stresses in elastic cylinders in contact along a generatrix," *Philosophical Magazine*, vol. 40, p. 454, 1949.

[9] H. Poritsky, "Stresses and deflections of cylindrical bodies in contact with application to contact of gears and of locomotive wheels," *Journal of Applied Mechanics*, vol. 17, pp. 191–201, 1950.

[10] J. Smith, "Stress due to tangential and normal loads on an elastic solid with application to some contact stress problems," *Journal of Applied Mechanics*, vol. 20, no. 2, pp. 157–166, 1953.

[11] G. Hamilton, "Explicit equations for the stresses beneath a sliding spherical contact," *Proceedings of the Institution of Mechanical Engineers, Part C: Journal of Mechanical Engineering Science*, vol. 197, no. 1, pp. 53–59, 1983.

[12] A. Sackfield and D. Hills, "Some useful results in the classical Hertz contact problem," *The Journal of Strain Analysis for Engineering Design*, vol. 18, no. 2, pp. 101–105, 1983.

[13] C. Truman, A. Sackfield, and D. Hills, "Contact mechanics of wedge and cone indenters," *International Journal of Mechanical Sciences*, vol. 37, no. 3, pp. 261–275, 1995.

[14] I. Green, "Poisson ratio effects and critical valus in spherical and cylindrical hertzian contacts," *APPLIED MECHANICS AND ENGINEERING*, vol. 10, no. 3, p. 451, 2005.

[15] D. Tabor, *The hardness of metals*. Oxford university press, 2000.

[16] H. Ghaednia, X. Wang, S. Saha, Y. Xu, A. Sharma, and R. L. Jackson, "A review of elastic–plastic contact mechanics," *Applied Mechanics Reviews*, vol. 69, no. 6, p. 060804, 2017.

[17] G. Dumas and C. Baronet, "Elastoplastic indentation of a half-space by an infinitely long rigid circular cylinder," *International journal of mechanical sciences*, vol. 13, no. 6, pp. 519–530, 1971.

[18] G. Care and A. Fischer-Cripps, "Elastic-plastic indentation stress fields using the finite-element method," *Journal of materials science*, vol. 32, no. 21, pp. 5653–5659, 1997.

[19] K. Komvopoulos, "Elastic-plastic finite element analysis of indented layered media," *Journal of Tribology*, vol. 111, no. 3, pp. 430–439, 1989.

[20] K. Komvopoulos, N. Saka, and N. Suh, "The role of hard layers in lubricated and dry sliding," *Journal of tribology*, vol. 109, no. 2, pp. 223–231, 1987.

[21] H. Tian and N. Saka, "Finite element analysis of an elastic-plastic two-layer half-space: sliding contact," *Wear*, vol. 148, no. 2, pp. 261–285, 1991.

[22] I. Anderson and I. Collins, "Plane strain stress distributions in discrete and blended coated solids under normal and sliding contact," *Wear*, vol. 185, no. 1-2, pp. 23–33, 1995.

[23] J. N. Kudva, "Overview of the DARPA smart wing project," *Journal of intelligent material systems and structures*, vol. 15, no. 4, pp. 261–267, 2004.

[24] S. Wax, G. Fischer, and R. Sands, "The past, present, and future of DARPAs investment strategy in smart materials," *JOM*, vol. 55, no. 12, pp. 17–23, 2003.

[25] H. Prahlad and I. Chopra, "Design of a variable twist tilt-rotor blade using shape memory alloy (SMA) actuators," in *Smart Structures and Materials 2001: Smart Structures and Integrated Systems*, vol. 4327, pp. 46–60, International Society for Optics and Photonics, 2001.

[26] D. J. Hartl and D. C. Lagoudas, "Aerospace applications of shape memory alloys," *Proceedings of the Institution of Mechanical Engineers, Part G: Journal of Aerospace Engineering*, vol. 221, no. 4, pp. 535–552, 2007.

[27] D. Mantovani, "Shape memory alloys: Properties and biomedical applications," *Jom*, vol. 52, no. 10, pp. 36–44, 2000.

[28] S. Thompson, "An overview of nickel–titanium alloys used in dentistry," *International endodontic journal*, vol. 33, no. 4, pp. 297–310, 2000.

[29] A. Andersen, D. Pedersen, A. Sivertsen, and S. Sangesland, "Detailed study of shape memory alloys in oil well applications," *SINTEF Petroleum Research, Trondheim, Norway, Tech. Rep*, vol. 32, pp. 00–01, 1999.

[30] H. Kahn, M. Huff, and A. Heuer, "The TiNi shape-memory alloy and its applications for MEMS," *Journal of Micromechanics and Microengineering*, vol. 8, no. 3, p. 213, 1998.

[31] R. Liu and D. Li, "A finite element model study on wear resistance of pseudoelastic TiNi alloy," *Materials Science and Engineering: A*, vol. 277, no. 1-2, pp. 169–175, 2000.

[32] Y. Luo, R. Liu, and D. Li, "Investigation of the mechanism for the improvement in wear resistance of nano-TiN/TiC/TiNi composite: a study combining experiment and FEM analysis," *Materials Science and Engineering: A*, vol. 329, pp. 768–773, 2002.

[33] G. Shaw, D. Stone, A. Johnson, A. Ellis, and W. Crone, "Shape memory effect in nanoindentation of nickel–titanium thin films," *Applied physics letters*, vol. 83, no. 2, pp. 257–259, 2003.

[34] R. Hill, *The mathematical theory of plasticity*, vol. 11. Oxford university press, 1998.

[35] R. Bishop, R. Hill, and N. Mott, "The theory of indentation and hardness tests," *Proceedings of the Physical Society*, vol. 57, no. 3, p. 147, 1945.

[36] K. Johnson, "The correlation of indentation experiments," *Journal of the Mechanics and Physics of Solids*, vol. 18, no. 2, pp. 115–126, 1970.

[37] A. M. Wood and T. Clyne, "Measurement and modelling of the nanoindentation response of shape memory alloys," *Acta materialia*, vol. 54, no. 20, pp. 5607–5615, 2006.

[38] F. Auricchio and R. L. Taylor, "Shape-memory alloys: modelling and numerical simulations of the finite-strain superelastic behavior," *Computer methods in applied mechanics and engineering*, vol. 143, no. 1-2, pp. 175–194, 1997.

[39] Y. Zhang, Y.-T. Cheng, and D. S. Grummon, "Finite element modeling of indentation-induced superelastic effect using a three-dimensional constitutive model for shape memory materials with plasticity," *Journal of Applied Physics*, vol. 101, no. 5, p. 053507, 2007.

[40] Y. Ivshin and T. J. Pence, "A thermomechanical model for a one variant shape memory material," *Journal of intelligent material systems and structures*, vol. 5, no. 4, pp. 455–473, 1994.

[41] W. Yan, "Theoretical investigation of wear-resistance mechanism of superelastic shape memory alloy NiTi," *Materials Science and Engineering: A*, vol. 427, no. 1-2, pp. 348–355, 2006.

[42] L. Wang, J. Xu, L. Yan, Z. Liu, and G. Yang, "A FEM study on the mechanical responses of pseudoelastic TiNi alloys to a particle normal loads," *Wear*, vol. 260, no. 6, pp. 573–579, 2006.

[43] C. Maletta, F. Furgiuele, E. Sgambitterra, M. Callisti, B. Mellor, and R. Wood, "Indentation response of a NiTi shape memory alloy: modeling and experiments," *Frattura ed Integrita Strutturale*, no. 21, pp. 5–12, 2012.

[44] I. Hutchings and P. Shipway, *Tribology: friction and wear of engineering materials*. Butterworth-Heinemann, 2017.

[45] D. Li, "Exploration of TiNi shape memory alloy for potential application in a new area: tribological engineering," *Smart Materials and Structures*, vol. 9, no. 5, p. 717, 2000.

[46] P. Clayton, "Tribological behavior of a titanium-nickel alloy," *Wear*, vol. 162, pp. 202–210, 1993.

[47] Y. Liang, S. Li, Y. Jin, W. Jin, and S. Li, "Wear behavior of a TiNi alloy," *Wear*, vol. 198, no. 1-2, pp. 236–241, 1996.

[48] H. Lin, J. He, K. Chen, H. Liao, and K. Lin, "Wear characteristics of TiNi shape memory alloys," *Metallurgical and Materials Transactions A*, vol. 28, no. 9, pp. 1871–1877, 1997.

[49] W. Ni, Y.-T. Cheng, and D. S. Grummon, "Microscopic superelastic behavior of a nickel-titanium alloy under complex loading conditions," *Applied Physics Letters*, vol. 82, no. 17, pp. 2811–2813, 2003.

[50] L. Qian, X. Xiao, Q. Sun, and T. Yu, "Anomalous relationship between hardness and wear properties of a superelastic nickel–titanium alloy," *Applied Physics Letters*, vol. 84, no. 7, pp. 1076–1078, 2004.

[51] M. Abedini, H. Ghasemi, and M. N. Ahmadabadi, "Tribological behavior of NiTi alloy in martensitic and austenitic states," *Materials & Design*, vol. 30, no. 10, pp. 4493–4497, 2009.

[52] L. Yan and Y. Liu, "Wear behavior of austenitic NiTi shape memory alloy," *Shape Memory and Superelasticity*, vol. 1, no. 1, pp. 58–68, 2015.

[53] D. Lagoudas, D. Hartl, Y. Chemisky, L. Machado, and P. Popov, "Constitutive model for the numerical analysis of phase transformation in polycrystalline shape memory alloys," *International Journal of Plasticity*, vol. 32, pp. 155–183, 2012.

[54] J. G. Boyd and D. C. Lagoudas, "A thermodynamical constitutive model for shape memory materials. part I. the monolithic shape memory alloy," *International Journal of Plasticity*, vol. 12, no. 6, pp. 805–842, 1996.

[55] Abaqus, "6.14 documentation," *Dassault Systemes Simulia Corporation*, 2014.

[56] J. Barlow, "Optimal stress locations in finite element models," *International Journal for Numerical Methods in Engineering*, vol. 10, no. 2, pp. 243–251, 1976.

[57] E. Kral and K. Komvopoulos, "Three-dimensional finite element analysis of surface deformation and stresses in an elastic-plastic layered medium subjected to indentation and sliding contact loading," *Journal of applied mechanics*, vol. 63, no. 2, pp. 365–375, 1996.

[58] W. Ni, Y.-T. Cheng, and D. S. Grummon, "Wear resistant self-healing tribological surfaces by using hard coatings on NiTi shape memory alloys," *Surface and Coatings Technology*, vol. 201, no. 3-4, pp. 1053–1057, 2006.

[59] W. Ni, Y.-T. Cheng, and D. S. Grummon, "Recovery of microindents in a nickel–titanium shape-memory alloy: a self-healing effect," *Applied physics letters*, vol. 80, no. 18, pp. 3310–3312, 2002.

[60] J. M. Nolan, D. J. Hartl, D. C. Lagoudas, and D. S. Grummon, "3D finite element analysis of indentation recovery due to the shape memory effect," in *Behavior and Mechanics of Multifunctional Materials and Composites 2010*, vol. 7644, p. 76440M, International Society for Optics and Photonics, 2010.

[61] P. K. Gupta and J. Walowit, "Contact stresses between an elastic cylinder and a layered elastic solid," *Journal of lubrication technology*, vol. 96, no. 2, pp. 250–257, 1974.

[62] R. King and T. O'sullivan, "Sliding contact stresses in a two-dimensional layered elastic half-space," *International Journal of Solids and Structures*, vol. 23, no. 5, pp. 581–597, 1987.

[63] Q. Kan, W. Yan, G. Kang, and Q. Sun, "Oliver–pharr indentation method in determining elastic moduli of shape memory alloysa phase transformable material," *Journal of the Mechanics and Physics of Solids*, vol. 61, no. 10, pp. 2015–2033, 2013.

[64] L.-L. Ke and Y.-S. Wang, "Two-dimensional contact mechanics of functionally graded materials with arbitrary spatial variations of material properties," *International Journal of Solids and Structures*, vol. 43, no. 18-19, pp. 5779–5798, 2006.

[65] X. Zhang, B. Xu, H. Wang, Y. Wu, and Y. Jiang, "Hertzian contact response of single-layer, functionally graded and sandwich coatings," *Materials & design*, vol. 28, no. 1, pp. 47–54, 2007.

[66] Y. Alinia, A. Beheshti, M. A. Guler, S. El-Borgi, and A. A. Polycarpou, "Sliding contact analysis of functionally graded coating/substrate system," *Mechanics of Materials*, vol. 94, pp. 142–155, 2016.